Biomechanics and Modeling in Mechanobiology (2026) 25:97
https://doi.org/10.1007/s10237-026-02121-2

ORIGINAL PAPER

Dynamic image-informed selection of biomechanical tumor growth models

Abdullah Al Noman[1] · Pratyush Kumar Singh[1] · David A. Hormuth II[2] · Danial Faghihi[1]

Received: 6 April 2026 / Accepted: 12 August 2026 / Published online: 31 August 2026
© The Author(s) 2026

Abstract

Glioblastoma progression is strongly influenced by evolving mechanical interactions between the tumor and surrounding brain tissue. However, the extent to which finite-deformation mechanics and constitutive assumptions improve subject-specific prediction as tumor burden evolves remains unclear. We introduce a sequential Bayesian inference and dynamic model selection framework that assimilates longitudinal murine magnetic resonance imaging (MRI) data to calibrate spatially varying tumor diffusivity, proliferation rate, and tissue stiffness in biomechanical tumor growth models. Competing formulations were compared at each imaging time, including reaction–diffusion without mechanics and reaction–diffusion coupled to linear elasticity or hyperelastic mechanics, using posterior model plausibility to adapt model choice for individualized one-scan-ahead prediction as new MRI scans are acquired. Across the studied animals, mechanically coupled models were consistently more plausible than the uncoupled reaction–diffusion model, and the evolution of model plausibility indicated an increasing role of mass effect and stress-mediated feedback of tumor growth during progression. While linear and hyperelastic coupled tumor growth models often produced similar tumor morphology, they yield distinct stress, deformation, and inferred stiffness fields, with the hyperelastic formulation often receiving higher posterior plausibility at later imaging times. These results indicate that, within the present longitudinal murine dataset, mechanical coupling is favored for image-informed glioma growth prediction and that constitutive assumptions should be evaluated sequentially for each subject rather than fixed a priori.

Keywords Biomechanical tumor growth · Finite deformation elasticity · Dynamic model selection · Image-informed modeling

1 Introduction

Glioblastoma (GBM), the most aggressive primary brain tumor, exhibits irregular and strongly subject-specific growth patterns driven by heterogeneous proliferation and invasion. A growing body of work in mechanobiology and biomechanics indicates that these patterns are governed by mechanical interaction with the confined brain and an evolving microenvironmental stiffness (Lucci et al. 2022; Ghahramani and Bavi 2026; Mpekris et al. 2015; Goriely et al. 2015). As GBM expands within the confined cranial cavity, solid stresses develop due to internal growth heterogeneity and external constraint from surrounding tissue. These stresses have been shown to modulate proliferation, compress vasculature, and promote invasive phenotypes through mechanotransduction (Helmlinger et al. 1997; Stylianopoulos et al. 2013; Jain et al. 2014; Mascheroni et al. 2016). Capturing this coupled tumor-tissue interaction is therefore central to predictive, biomechanical models of GBM progression and to mechanistic interpretation of growth patterns observed in longitudinal imaging (Lucci et al. 2022; Ghahramani and Bavi 2026).

Many current continuum tumor growth models for predicting GBMs rely on reaction–diffusion (RD) formulations (Swanson et al. 2000) that represent proliferation and invasion but do not explicitly account for mass effect. Mechanically coupled extensions have incorporated deformation by coupling RD dynamics to small-strain linear elasticity

✉ Danial Faghihi
danialfa@buffalo.edu

[1] Department of Mechanical and Aerospace Engineering, University at Buffalo, Buffalo, NY, USA

[2] Oden Institute for Computational Engineering and Sciences, Livestrong Cancer Institutes, University of Texas at Austin, Austin, TX, USA

mechanics and calibrating model parameters from imaging data (Tunç et al. 2021; Hormuth et al. 2017; Hogea et al. 2007; Lima et al. 2016). More recent biomechanics models have introduced more comprehensive descriptions, including multiphase models coupled with finite-deformation elasticity, to better represent soft-tissue mechanics and quantify growth-induced stress and deformation (Faghihi et al. 2020; Wong et al. 2014; Lucci et al. 2022). Despite recent progress in image-driven GBM modeling, a key scientific gap is the choice of constitutive assumptions are typically imposed *a priori*. Most studies calibrate a single chosen formulation and assess performance primarily through morphology-based agreement with the imaging data, without dynamically updating the underlying mechanical description. In particular, existing Bayesian calibration studies have primarily focused on estimating parameters within a prescribed tumor growth model, whereas the present question is whether the biomechanical model itself remains plausible as subject-specific longitudinal data are assimilated. Thus, the gap addressed here is not Bayesian calibration alone, but sequential, subject-specific comparison of competing biomechanical models using posterior model plausibility. Given the subject-specific and evolving nature of GBM growth, it remains unclear how strongly longitudinal imaging data support mechanical coupling, and whether linear elastic or hyperelastic mechanical assumptions are more plausible for a given subject as tumor burden evolves. These limitations motivate a dynamic model selection framework capable of choosing between competing biomechanical models as longitudinal data accumulate. Here, the dynamic model selection refers to sequential updating of posterior model plausibility as new longitudinal imaging data are assimilated, not to automatic discovery of new model forms. At each assimilation time, candidate competing models specified *a priori* are recalibrated using the accumulated MRI data from a given animal, their posterior model probabilities are recomputed, and the most plausible model can be used for individualized one-scan-ahead prediction.

In this work, we address these gaps by developing an image-driven framework for sequential Bayesian inference and dynamic selection of biomechanical glioma growth models. The present study builds on prior murine glioma imaging studies in which MRI-constrained reaction–diffusion models were personalized to individual animals and subsequently extended through linear-elastic mechanical coupling to improve prediction under mass-effect constraints (Hormuth et al. 2015, 2017). It also extends our earlier Bayesian inference framework for estimating spatially varying tumor-growth parameters from MRI data (Liang et al. 2023). While that work focused on calibrating heterogeneous parameter fields within a prescribed tumor-growth model, the present study develops a scalable formulation for computing posterior model plausibility and uses it to compare competing biomechanical model hypotheses sequentially as new longitudinal MRI data are assimilated. Longitudinal MRI data from preclinical murine glioma subjects are used to update subject-specific fields of tumor diffusivity, proliferation rate, and tissue stiffness, while also quantifying uncertainty in the inferred high-dimensional parameter space. Instead of prescribing a fixed biomechanical formulation, we compare three candidate models: reaction–diffusion without mechanics, reaction–diffusion coupled with linear elasticity, and reaction–diffusion coupled with hyperelastic mechanics. We focus on these parsimonious reaction–diffusion-based formulations because the available MRI-derived tumor volume fraction data directly constrain proliferation, invasion, and mechanically mediated deformation more strongly than additional biological compartments such as necrosis or apoptosis. Posterior model plausibility is recomputed at each assimilation time, enabling subject-specific model selection for one-scan-ahead prediction as new MRI scans become available. Using longitudinal murine glioma data, we show that mechanically coupled models are favored over the uncoupled RD model in the present dataset, while the relative support for linear elastic versus hyperelastic mechanics evolves across animals and imaging times. These results position posterior model plausibility as a mechanics-informed criterion for adapting biomechanical tumor growth predictions from longitudinal imaging data, beyond morphology agreement alone.

The remainder of the paper is organized as follows. Section 2 describes the longitudinal murine glioma MRI data, the biomechanical tumor growth model, the MRI-informed sequential Bayesian inference framework, and the dynamic model selection theory based on posterior plausibility, including scalable solution and computation of model evidence. Section 3 reports the prior specification and hyper-parameter selection, presents sequential subject-specific calibration and sequential predictions, and time-resolved model plausibility across the competing biomechanical computational models. Finally, Sect. 4 discusses the biomechanical implications of the results, limitations, and directions for future extensions toward more comprehensive mechanics-informed tumor growth modeling.

2 Methods

2.1 Imaging data in murine glioma

Longitudinal magnetic resonance imaging (MRI) data of glioma growth in female Wistar rats were obtained from previously published murine glioma imaging and modeling studies (Hormuth et al. 2017, 2015; Hormuth 2016; Hormuth et al. 2014). Tumors were established via stereotaxic injection of 10^5 C6 glioma cells into the neocortex. MRI data were acquired at multiple time points after tumor implantation

using a 9.4T preclinical MRI system with a 38-mm-diameter Litz quadrature coil (Doty Scientific). For each scan, the imaged volume was $32,\text{mm} \times 32,\text{mm} \times 16,\text{mm}$, discretized on a $128 \times 128 \times 16$ image grid, corresponding to voxels of size $0.25,\text{mm} \times 0.25,\text{mm} \times 1,\text{mm}$. All longitudinal scans for a given animal were rigidly registered to the earliest scan using mutual information to maintain spatial correspondence across time.

Multiple MRI modalities were used to construct the computational model and define the data for sequential Bayesian inference. T_2-weighted images (fast spin echo sequence with $TR = 2000$ ms and $TE = 30$ ms) were used to define the brain geometry and computational domain, while contrast-enhanced T_1-weighted images (spoiled gradient echo sequence with $TR = 45$ ms, $TE = 1.4$ ms, and $\alpha = 20°$) were used to delineate tumor burden. Diffusion-weighted MRI ($TR = 2000$ ms, $TE = 30$ ms, b-values of 0, 300, 500, 700, 800, and 1100 s/mm^2, $\Delta = 25$ ms, and $\delta = 2$ ms) was used to derive apparent diffusion coefficient (ADC) maps (Padhani et al. 2009). The primary imaging outputs used in the present analysis were segmented tumor regions, ADC maps, contrast-enhanced T_1-weighted images, and T_2-weighted images. Additional MRI-derived quantities, including T_1 maps and dynamic contrast-enhanced MRI maps, were acquired in the original studies but were not used here. Full details of the animal experiments, image acquisition, preprocessing, and original image-based modeling analyses are provided in Hormuth et al. (2017, 2015); Hormuth (2016). ADC maps were used as an indirect measure of local tumor cellularity. ADC quantifies the diffusion of free water molecules within tissue and is restricted by microstructural barriers such as cell membranes. Consequently, an inverse relationship between ADC and cellular density has been reported in tumor imaging studies (Sugahara et al. 1999; Anderson et al. 2000; Barnes et al. 2015; Atuegwu et al. 2011), supporting the use of ADC as a first-order surrogate for local tumor cell burden within the segmented tumor region. Following established protocols (Hormuth et al. 2017, 2015), ADC measurements were converted into spatially resolved estimates of tumor cell density. The resulting cell-density estimates were normalized by a voxel-dependent carrying capacity, taken as the local upper bound on tumor cell concentration. This normalization yields a dimensionless tumor volume fraction field at multiple time points, which serves as the primary data quantity for calibrating spatiotemporal tumor growth and assessing the evolving mechanical interaction between the growing tumor and host tissue.

In the present work, longitudinal imaging data from four animals are considered. The imaging time points, measured in days after tumor implantation, are as follows: Rat I: 12, 14, 15, 16, 19, and 21 days; Rat II: 10, 12, 14, 15, 16, and 18 days; Rat III: 10, 12, 14, 15, 16, and 19 days; and Rat IV: 10, 12, 14, 16, 18, and 20 days. The 10 to 21 day imaging window was determined by the earliest time at which tumors were consistently visible on MRI and by mandatory humane endpoints associated with rapid C6 glioma growth. All animal procedures were approved by the appropriate Institutional Animal Care and Use Committee, as detailed in the original experimental studies (Hormuth et al. 2017, 2015). The present analysis is conducted on a selected axial slice containing the primary tumor burden. Because the MRI slice thickness is approximately four times larger than the in-plane resolution, the selected axial slice represents a finite-thickness slab through the tumor region. The resulting two-dimensional analysis is therefore interpreted as a slice-based approximation, with explicit through-plane deformation and full volumetric tumor mechanics left to future three-dimensional inference.

2.2 Biomechanical tumor growth models

The widely used continuum models to describe tissue-scale glioma growth is reaction–diffusion (RD) models consisting of the proliferation-infiltration representation of tumor evolution through the combined effects of local proliferation and spatial invasion (Swanson et al. 2000). However, such models neglect the mechanical interactions between the growing tumor and the surrounding brain tissue. Mechanical stresses generated during tumor expansion can suppress proliferation, alter transport processes, and induce deformation of healthy tissue, commonly referred to as mass effect. Previous mechanically coupled models have often represented these effects using small-strain linear elasticity (Hormuth et al. 2017; Tunç et al. 2021; Hogea et al. 2007), incorporating tumor-induced tissue deformation and stress-mediated growth modulation. In contrast, the present work extends this class of mechanically coupled RD models by incorporating finite-strain tissue mechanics through a hyperelastic constitutive relation. Our ultimate goal is the calibration of biomechanical tumor growth models using longitudinal MRI data. Since all MRI scans acquired at later time points are rigidly registered to the first imaging time point and the finite element mesh is constructed from the corresponding initial brain geometry, it is natural and computationally convenient to formulate and solve the coupled governing equations in a Lagrangian (reference) configuration.

Let $\phi(\mathbf{X}, t) \in [0, 1]$ denote the tumor volume fraction defined over the reference configuration Ω_0, where $\mathbf{X}$ is the material coordinate. The coupled system governing tumor growth and tissue deformation is given by

$$J\frac{\partial \phi}{\partial t} = \nabla_0 \cdot \left(JD\, e^{-Hp_\tau} \quad \mathbf{F}^{-1}\mathbf{F}^{-T}\nabla_0 \phi\right) + JG(1-\phi)\phi \quad \text{in } \Omega_0 \times (0,T], \tag{1}$$

$$\nabla_0 \cdot \mathbf{P} = CJ\mathbf{F}^{-T}\nabla_0 \phi \ \text{ in } \Omega_0 \times (0,T], \tag{2}$$

together with the boundary and initial conditions

$$\begin{aligned} \left(JDe^{-Hp_\tau}\mathbf{F}^{-1}\mathbf{F}^{-T}\nabla_0\phi\right)\cdot \mathbf{N} &= 0 \text{ on } \partial\Omega_0 \times (0,T], \\ \mathbf{u} &= \mathbf{0} \text{ on } \partial\Omega_0 \times (0,T], \\ \phi(\mathbf{X},0) &= \phi_0(\mathbf{X}) \text{ in } \Omega_0. \end{aligned} \tag{3}$$

Here, $\mathbf{u}$ is the displacement field, $\mathbf{F} = \mathbf{I} + \nabla_0\mathbf{u}$ is the deformation gradient, and Jacobian $J = \det(\mathbf{F})$ represents the local volume change. The tensor $\mathbf{P}$ denotes the first Piola–Kirchhoff stress, $\nabla_0(\cdot)$ is the gradient with respect to the reference configuration, and $\mathbf{N}$ is the outward unit normal on $\partial\Omega_0$. Mechanical stress enters the tumor growth model through the scalar quantity $p_\tau := -\frac{1}{3}\operatorname{tr}(\boldsymbol{\tau})$, where $\boldsymbol{\tau}$ is the Kirchhoff stress tensor. The quantity p_τ represents a measure of local mean compressive stress and provides a scalar, frame-invariant description of mechanical loading suitable for use in a Lagrangian formulation.

The first partial differential equation (PDE) in 1 is the Lagrangian form of a reaction–diffusion balance law for tumor volume fraction, where the factors involving J and $\mathbf{F}^{-1}\mathbf{F}^{-T}$ arise from mapping diffusion from the deformed configuration to the reference configuration. The logistic source term $G(1-\phi)\phi$ represents local tumor proliferation adopted from (Swanson et al. 2000; Hormuth et al. 2015). The present formulation does not explicitly include necrosis, apoptosis, or additional cellular compartments. It is intentionally restricted to a parsimonious model whose spatially varying parameters can be constrained and informed by the available MRI-derived tumor volume fraction data. The second PDE in 2 represents quasi-static mechanical equilibrium of the deforming tissue, where tumor expansion induces a mass-effect driving term proportional to the spatial gradient of tumor volume fraction. For the associated boundary and initial conditions in (3), the zero-flux condition for ϕ represents no net tumor-cell flux across the outer boundary of the computational brain domain. The displacement condition $\mathbf{u} = 0$ on $\partial\Omega_0$ provides a simplified representation of the mechanical confinement imposed by the surrounding cranial environment and skull. The initial condition ϕ_0 is obtained from the first MRI-derived tumor volume fraction field. The model parameters are D denoting the baseline tumor cell diffusivity, H controls the sensitivity of diffusion to mechanical stress, G is the proliferation rate, and C is a coupling parameter governing the magnitude of tumor-induced mass effect. The reaction–diffusion and mechanical partial differential equations are coupled through two mechanisms: (i) *stress-modulated diffusivity*, where cell motility decreases exponentially with increasing compressive stress, modeled through the Kirchhoff stress invariant p_τ, which captures the inhibitory effect of mechanical confinement on cell migration; and (ii) *mass effect*, represented phenomenologically by a pressure-like body force proportional to the tumor volume fraction gradient, which drives deformation of the surrounding tissue.

To enable calibration from single-slice MRI data, we adopt a plane-strain approximation of a three-dimensional compressible Neo-Hookean material. This approximation permits controlled comparison of constitutive assumptions in the selected slice, but does not capture out-of-plane deformation. The strain-energy density function is defined as

$$W(\mathbf{B}) = \frac{S}{2}\left(\operatorname{tr}\left(J^{-2/3}\mathbf{B}\right) - 3\right) + \frac{K}{2}(J-1)^2,$$

where $\mathbf{B} = \mathbf{F}\mathbf{F}^T$ is the left Cauchy–Green deformation tensor. The parameters S and K denote the shear and bulk moduli, respectively, and are related to Young's modulus E and Poisson's ratio ν by $S = \frac{E}{2(1+\nu)}, K = \frac{E}{3(1-2\nu)}$. The first Piola–Kirchhoff stress tensor is obtained from the strain-energy density function as $\mathbf{P} = \frac{\partial W}{\partial \mathbf{F}}$. For the compressible Neo-Hookean model defined above, this yields the explicit expression

$$\mathbf{P} = SJ^{-2/3}\left(\mathbf{F} - \frac{1}{3}\operatorname{tr}(\mathbf{B})\mathbf{F}^{-T}\right) + KJ(J-1)\mathbf{F}^{-T}. \tag{4}$$

2.3 Image-informed sequential Bayesian inference

Longitudinal MRI provides subject-specific observations of tumor evolution over time, enabling individualized prediction of tumor growth and biophysical parameters dynamics using computational models. As imaging measurements become available sequentially, Bayesian filtering offers a principled framework for updating model parameters, propagating uncertainty through the coupled growth–mechanics model, and quantifying the reliability of subject-specific predictions. Since the inferred tumor volume fraction field reflects both mechanically mediated proliferative and infiltration growth, accurate prediction of tumor shape and spatial extent is essential for resolving biomechanical heterogeneity. To this end, we formulate an image-informed sequential Bayesian inference framework with spatially varying parameters, allowing longitudinal MRI data to update both the temporal evolution and spatial structure of growth and mechanical parameter fields.

Let $\boldsymbol{d}^{(1:k)} = \{d(\mathbf{X},t_1),\ldots,d(\mathbf{X},t_k)\}$ denote the sequence of imaging-derived tumor volume fraction fields acquired up to time t_k, with all images registered to the reference configuration Ω_0 defined by the first imaging time point. Let $\boldsymbol{\theta}^{(k)} = \boldsymbol{\theta}(\mathbf{X},t_k) \in \Theta$ denote the model parameter vector

at time t_k, which includes spatially varying growth, diffusion, and mechanical coefficients of the biomechanical tumor growth model. Here, the superscript k denotes the assimilation step and conditioning on data available up to t_k, and no explicit temporal evolution law is prescribed for the parameter fields. The sequential Bayesian filtering consists of updating the posterior distribution of the model parameters as new imaging data become available. At time t_k, the posterior probability distribution function (PDF) is given by,

$$\pi_{\text{post}}\left(\boldsymbol{\theta}^{(k)} \mid \boldsymbol{d}^{(1:k)}\right) = \frac{\pi_{\text{like}}\left(\boldsymbol{d}^{(1:k)} \mid \boldsymbol{\theta}^{(k)}\right)\pi_{\text{pr}}(\boldsymbol{\theta})}{\pi_{\text{evid}}\left(\boldsymbol{d}^{(1:k)}\right)}, \tag{5}$$

where $\pi_{\text{pr}}(\boldsymbol{\theta})$ denotes the prior PDF, $\pi_{\text{like}}(\boldsymbol{d}^{(1:k)} \mid \boldsymbol{\theta}^{(k)})$ is the likelihood function, and $\pi_{\text{evid}}(\boldsymbol{d}^{(1:k)})$ is the evidence PDF. Given the posterior distribution at time t_k, a predictive distribution for the tumor state at the next time point t_{k+1} is obtained by propagating parameter uncertainty through the biomechanical tumor growth model,

$$\pi\left(\phi^{(k+1)} \mid \boldsymbol{d}^{(1:k)}\right) = \int_{\Theta} \pi\left(\phi^{(k+1)} \mid \boldsymbol{\theta}^{(k)}\right) \pi_{\text{post}}\left(\boldsymbol{\theta}^{(k)} \mid \boldsymbol{d}^{(1:k)}\right) \mathrm{d}\boldsymbol{\theta}, \tag{6}$$

where $\phi^{(k+1)} = \phi(\mathbf{X}, t_{k+1})$ denotes the tumor volume fraction field at the future prediction time. This *one-scan-ahead* prediction is continued as new longitudinal imaging data are acquired, enabling sequential refinement of model parameters and tumor growth predictions.

To enable spatially varying Bayesian inference, the model parameter fields are discretized over the finite element mesh defined on the reference configuration Ω_0. A Gaussian random field prior is imposed on the discretized parameter vector $\boldsymbol{\theta} \sim \mathcal{N}(\bar{\boldsymbol{\theta}}, \boldsymbol{\Gamma}_{\text{pr}})$, where $\bar{\boldsymbol{\theta}}$ denotes the prior mean field and $\boldsymbol{\Gamma}_{\text{pr}}$ is a covariance matrix corresponding to a Matérn class. Following (Roininen et al. 2014; Tan and Faghihi 2024; Liang et al. 2023; Singh and Faghihi 2025), such Gaussian random field can be equivalently defined as the solution of the following stochastic partial differential equation,

$$\begin{aligned} -\gamma\Delta_0\boldsymbol{\theta} + \delta\boldsymbol{\theta} &= \dot{\boldsymbol{W}}, \text{ in } \Omega_0, \\ \boldsymbol{\theta} + \beta\nabla_0\boldsymbol{\theta}\cdot\mathbf{N} &= 0, \text{ on } \partial\Omega_0, \end{aligned} \tag{7}$$

where $\dot{\boldsymbol{W}}$ denotes spatial Gaussian white noise, Δ_0 is the Laplacian operators with respect to the reference configuration, and $\mathbf{N}$ is the outward unit normal on $\partial\Omega_0$. The parameters δ and γ control the marginal variance σ^2 and correlation length ρ of the prior field through $\delta = \frac{\sqrt{2}}{\sigma\rho\sqrt{\pi}}$ and $\gamma = \frac{1}{4\sqrt{2\pi}}\frac{\rho}{\sigma}$, while the Robin boundary coefficient is set as $\beta = \frac{\sqrt{\delta\gamma}}{1.42}$, which mitigates boundary artifacts arising from truncation of the spatial domain (Daon and Stadler 2016). The choice of Gaussian random field prior the spatially varying parameter fields is because it provides a tractable way to encode expected spatial smoothness, marginal variability, and correlation length scales of the biophysical parameters. This prior also regularizes the high-dimensional inverse problem and reduces nonphysical spatial oscillations in regions weakly informed by the imaging data. Although the true parameter fields need not to be Gaussian, the Gaussian prior provides a computationally efficient and widely used representation for Bayesian inverse problems with spatially correlated parameters (Alghamdi et al. 2021; Liang et al. 2023; Villa et al. 2021). The likelihood function is defined through an additive noise model relating imaging-derived observations to model predictions. Assuming zero-mean, Gaussian noise with variance σ^2_{noise} to account for both model and measurement errors, the likelihood function associated with the cumulative imaging data $\boldsymbol{d}^{(1:k)}$ is given by

$$\pi_{\text{like}}\left(\boldsymbol{d}^{(1:k)} \middle| \boldsymbol{\theta}^{(k)}\right) \propto \exp -\left(\sum_{i=1}^{k} \frac{1}{2\sigma^2_{\text{noise}}} \int_{\Omega_0} \left[\phi(\mathbf{X}, t_i; \boldsymbol{\theta}^{(k)}) - d(\mathbf{X}, t_i)\right]^2 \mathrm{d}\mathbf{X}\right). \tag{8}$$

The MRI-derived tumor volume fraction fields $\boldsymbol{d}$ are therefore not treated as exact ground truth observation of tumor. The Gaussian noise variance σ^2_{noise} represents an aggregate observation uncertainty that includes MRI measurement noise, image registration and segmentation errors, and residual model discrepancy.

2.4 Dynamic tumor growth model selection

A variety of tumor growth models have been proposed to describe GBM evolution, differing in their biological realism, mechanical fidelity, and number of parameters. The biomechanical tumor growth model described in Sect. 2.2 represents one such formulation. Alternative choices include more detailed hyperelastic constitutive descriptions of brain tissue, e.g., (Budday et al. 2015; Mihai et al. 2017), simplified mechanical representations based on linear elasticity (Hormuth et al. 2017), and purely reaction-diffusion models that neglect tissue deformation altogether (Swanson et al. 2000). Each model emphasizes different aspects of tumor progression and may be more appropriate under different stages of growth and mechanically mediated mass effect. However, the adequacy of a prescribed biomechanical formulation may change as longitudinal data are assimilated and tumor burden evolves. Mechanical effects may be limited during early infiltrative growth but become more influential as stress builds and deformation of the surrounding tissue emerges. Relying on a fixed model without reassessing its support can therefore reduce mechanistic fidelity and predictive reliability. To address

this limitation, we adopt a dynamic Bayesian model selection framework in which longitudinal MRI data from an individual subject are used to quantify the relative plausibility of competing tumor growth models.

Let $\{M_1, \ldots, M_m\}$ denote a set of competing tumor growth models. At imaging time t_k, model plausibility is quantified through the posterior probability of the discrete model variable conditioned on the cumulative imaging data $\boldsymbol{d}^{(1:k)}$. Given a prior probability mass function over models, $\pi_{\text{pr}}(M)$, the posterior model probabilities are given by

$$\pi\big(M_i \mid \boldsymbol{d}^{(1:k)}\big) = \frac{\pi_{\text{evid}}\big(\boldsymbol{d}^{(1:k)} \mid M_i\big)\, \pi_{\text{pr}}(M_i)}{\sum_{j=1}^{m} \pi_{\text{evid}}\big(\boldsymbol{d}^{(1:k)} \mid M_j\big)\, \pi_{\text{pr}}(M_j)}, \qquad i = 1, \ldots, m. \tag{9}$$

Here, $\pi_{\text{evid}}(\boldsymbol{d}^{(1:k)} \mid M_i)$ denotes the model evidence (marginal likelihood) under model M_i, obtained by marginalizing over the corresponding model parameters,

$$\pi_{\text{evid}}\big(\boldsymbol{d}^{(1:k)} \mid M_i\big) = \int_{\Theta_i} \pi_{\text{like}}\big(\boldsymbol{d}^{(1:k)} \mid \boldsymbol{\theta}_i, M_i\big)\ \pi_{\text{pr}}\big(\boldsymbol{\theta}_i \mid M_i\big)\, \mathrm{d}\boldsymbol{\theta}_i, \tag{10}$$

where Θ_i denotes the parameter space associated with model $\mathcal{M}_i$. In this setting, as additional imaging data become available, the posterior model probabilities $\pi\Big(M_i^{(k)} \mid \boldsymbol{d}^{(1:k)}\Big)$ are updated sequentially, allowing longitudinal MRI measurements to change the relative support for candidate models over time. In particular, for each animal, this evidence calculation is repeated at each assimilation time using all MRI data available up to that time. The resulting posterior model probabilities define a subject-specific, time-updated ranking of the candidate models, which can be used to select the model for the subsequent one-scan-ahead prediction.

2.5 Scalable Bayesian filtering and model plausibility

Finite element discretization of the spatially varying growth and mechanical parameter fields yields a high-dimensional parameters $\boldsymbol{\theta} \in \mathbb{R}^{N_p}$, rendering Bayesian inference computationally intractable with standard methods. To address this challenge, we employ scalable Bayesian solution strategies whose computational cost in terms of number of model solves is independent of the parameter dimension.

1) Laplace approximation (LA) of the posterior

The primary solution strategy is a Laplace approximation of the Bayesian filtering posterior, obtained by locally approximating the posterior distribution in (5) with a Gaussian centered at the maximum a posteriori (MAP) estimate. At each assimilation step, defined here as the Bayesian update performed when a new MRI scan becomes available, the posterior is approximated as, $\pi_{\text{post}}(\boldsymbol{\theta}^{(k)} \mid \boldsymbol{d}^{(1:k)}) \approx \mathcal{N}(\boldsymbol{\theta}_{\text{MAP}}^{(k)}, \boldsymbol{\Gamma}_{\text{post}}^{(k)})$. The MAP estimate is computed by minimizing the negative log-posterior,

$$\boldsymbol{\theta}_{\text{MAP}}^{(k)} = \arg\min_{\boldsymbol{\theta}} \left\{ \frac{1}{2\sigma_{\text{noise}}^2} \sum_{i=1}^{k} \int_{\Omega_0} \big[\phi(\mathbf{X}, t_i; \boldsymbol{\theta}) - d(\mathbf{X}, t_i)\big]^2 \mathrm{d}\mathbf{X} + \frac{1}{2} \big\|\boldsymbol{\theta} - \overline{\boldsymbol{\theta}}\big\|^2_{\boldsymbol{\Gamma}_{\text{pr}}^{-1}} \right\}, \tag{11}$$

which balances data misfit with the Gaussian random field prior. This optimization problem is solved using a globalized inexact Newton–CG method with adjoint-based gradient and Hessian–vector evaluations, combined with a backtracking line search to ensure global convergence (Villa et al. 2021). The posterior covariance is given by

$$\boldsymbol{\Gamma}_{\text{post}}^{(k)} = \Big(\boldsymbol{H}_{\text{misfit}}\Big(\boldsymbol{\theta}_{\text{MAP}}^{(k)}\Big) + \boldsymbol{\Gamma}_{\text{pr}}^{-1} \Big)^{-1}, \tag{12}$$

where $\boldsymbol{H}_{\text{misfit}}$ denotes the Hessian of the data misfit term. Exploiting the rapid decay of the generalized eigenvalues $\{\lambda_i\}$ of the data misfit Hessian with respect to the prior precision, we retain only the leading $r \ll N_p$ modes, yielding the low-rank approximation

$$\boldsymbol{\Gamma}_{\text{post}}^{(k)} \approx \boldsymbol{\Gamma}_{\text{pr}} - \ \boldsymbol{W}_r \boldsymbol{D}_r \boldsymbol{W}_r^T, \tag{13}$$

where $\boldsymbol{D}_r = \text{diag}\big(\lambda_i/(1+\lambda_i)\big)$ and the columns of $\boldsymbol{W}_r$ are the dominant generalized eigenvectors. This low-rank structure enables scalable Bayesian filtering whose dominant cost depends only weakly on the parameter dimension and is governed primarily by the number of retained Hessian modes and the underlying forward and adjoint solves (Isaac et al. 2015; Kim et al. 2023; Villa et al. 2021).

In this work, the Laplace approximation framework is further extended to enable scalable evaluation of the posterior model plausibility defined in (9). For each candidate model $\{M_i\}_{i=1}^m$, the model evidence conditioned on the cumulative imaging data $\boldsymbol{d}^{(1:k)}$ is approximated as

$$\begin{aligned} \log \pi_{\text{evid}}\big(\boldsymbol{d}^{(1:k)} | M_i\big) \approx & -\Phi_i\Big(\boldsymbol{\theta}_{\text{MAP},i}^{(k)}\Big) \\ & - \frac{1}{2}\big\|\boldsymbol{\theta}_{\text{MAP},i}^{(k)} - \overline{\boldsymbol{\theta}}_i\big\|^2_{\boldsymbol{\Gamma}_{\text{pr},i}^{-1}} - \frac{N_d}{2} \log\big(2\pi\sigma_{\text{noise}}^2\big) \\ & - \frac{1}{2}\sum_{j=1}^{r_i} \log(1+\lambda_{i,j}), \end{aligned} \tag{14}$$

where $\boldsymbol{\theta}_{\text{MAP},i}^{(k)}$ denotes the MAP estimate under model M_i, Φ_i is the corresponding data misfit functional, N_d is number of data points, $\boldsymbol{\Gamma}_{\text{pr},i}$ is the prior covariance associated with M_i, and $\{\lambda_{i,j}\}_{j=1}^{r_i}$ are the dominant generalized eigenvalues of the data misfit Hessian. Full derivations of the Laplace-approximated posterior and model evidence are provided in the *Supplementary Information*. Substituting the approximated evidences (14) into (9)

yields a scalable approximation of the posterior model plausibility. In the absence of prior preference among competing models, i.e., $\pi_{\text{pr}}(M_i) = \frac{1}{m}$, the posterior model probabilities reduce to the normalized model evidences,

$$\pi(M_i \mid \boldsymbol{d}^{(1:k)}) = \frac{\pi_{\text{evid}}(\boldsymbol{d}^{(1:k)} \mid M_i)}{\sum_{j=1}^{m} \pi_{\text{evid}}(\boldsymbol{d}^{(1:k)} \mid M_j)}, \qquad i = 1, \dots, m. \tag{15}$$

2) Dimension-independent Markov chain Monte Carlo (MCMC)

Although the Laplace approximation enables scalable Bayesian filtering, its reliance on local linearization about the MAP estimate may lead to inaccuracies when the posterior distribution exhibits strong non-Gaussian structure. To assess the accuracy of the LA, we compare its results against a sampling-based reference solution using dimension-independent MCMC. We employ the generalized preconditioned Crank–Nicolson (gpCN) algorithm. The pCN method (Cotter et al. 2013) is well-defined in infinite-dimensional parameter spaces and exhibits dimension-independent mixing when sampling Gaussian measures, but in PDE-constrained inverse problems it is often sensitive to step-size selection, leading to poor acceptance rates and high autocorrelation. The gpCN algorithm (Pinski et al. 2015) overcomes these limitations by incorporating local posterior geometry through the MAP estimate and posterior covariance obtained from the Laplace approximation. This results in improved sampling efficiency while retaining dimension-independent scalability (Alghamdi et al. 2021; Kim et al. 2023). The gpCN algorithm used to sample the posterior associated with one Bayesian update in (5) is summarized in Algorithm 1. In Algorithm 1, the posterior ratio is evaluated with respect to the Gaussian reference measure $\mathcal{N}(\boldsymbol{\theta}_{\text{MAP}}, \boldsymbol{\Gamma}_{\text{post}})$ used in the gpCN proposal, equivalently including the corresponding proposal density correction in the acceptance ratio.

Algorithm 1 Generalized preconditioned Crank-Nicolson (gpCN) sampler for one update of the Bayesian filter.

Require: MAP estimate $\boldsymbol{\theta}_{\text{MAP}}$, posterior covariance $\boldsymbol{\Gamma}_{\text{post}}$, step size $s \in (0, 1)$, chain length L, initial state $\boldsymbol{\theta}^0$

Set $\ell \leftarrow 0$
while $\ell \leq L - 1$ **do**
  Draw $\boldsymbol{\xi}^{\ell} \sim \mathcal{N}(\mathbf{0}, \boldsymbol{\Gamma}_{\text{post}})$
  $\boldsymbol{\theta}^{\star} \leftarrow \boldsymbol{\theta}_{\text{MAP}} + \sqrt{1 - s^2}\,(\boldsymbol{\theta}^{\ell} - \boldsymbol{\theta}_{\text{MAP}}) + s\,\boldsymbol{\xi}^{\ell}$
  $\alpha \leftarrow \min\left(1, \frac{\pi_{\text{post}}(\boldsymbol{\theta}^{\star} \mid \boldsymbol{d})}{\pi_{\text{post}}(\boldsymbol{\theta}^{\ell} \mid \boldsymbol{d})}\right)$
  Draw $u \sim \mathcal{U}(0, 1)$. If $u \leq \alpha$ set $\boldsymbol{\theta}^{\ell+1} \leftarrow \boldsymbol{\theta}^{\star}$; else set $\boldsymbol{\theta}^{\ell+1} \leftarrow \boldsymbol{\theta}^{\ell}$
  $\ell \leftarrow \ell + 1$
end while
return $\{\boldsymbol{\theta}^{\ell}\}_{\ell=1}^{L}$

3 Results

We present results from sequential Bayesian inference of the biomechanically coupled tumor growth model introduced in Sect. 2.2, using longitudinal MRI data from murine glioma subjects described in Sect. 2.1. The focus is to quantify how mechanical coupling and constitutive assumptions influence model plausibility, inferred parameter fields, and predictive performance. All simulations are performed in two spatial dimensions (2D) using the central axial slice along the cranial–caudal direction. This slice was selected because it contained the dominant MRI-derived tumor burden over the longitudinal imaging window. A slice selection analysis and an adjacent slice inference check are reported in the *Supplementary Information*, supporting that the tumor area and model plausibility trends are not artifacts of the selected slice. Although MRI-driven 3D Bayesian inference has been demonstrated previously (Liang et al. 2023), restricting the present analysis to 2D enables a controlled and computationally feasible comparison between LA and gpCN Bayesian inference, and the resulting mechanics should therefore be interpreted as slice-based rather than fully three-dimensional. For each subject, T_2-weighted MRI are used to construct the finite element mesh over the domain Ω_0. The tumor volume fraction at the first scan defines the initial condition $\phi_0(\boldsymbol{X})$, with DW-MRI data interpolated to mesh nodes. At each imaging time, data up to that scan are assimilated via Bayesian filtering, followed by a *one-scan-ahead* prediction to the subsequent MRI time point. The main analysis focuses on one-scan-ahead prediction because the framework is

designed for sequential data assimilation; a multi-step prediction experiment without intermediate data assimilation is provided in the *Supplementary Information* to assess degradation over longer forecast horizons. Dynamic model selection is performed separately for each animal by evaluating the posterior plausibility of three candidate formulations specified *a priori*: reaction–diffusion without mechanics, reaction–diffusion coupled with linear elasticity, and reaction–diffusion coupled with hyperelastic mechanics. Thus, model plausibility is updated as each animal's MRI time series is assimilated and can be used to adapt the one-scan-ahead prediction model. Predictive agreement is quantified using the Dice similarity coefficient and normalized tumor area (NTA). The Dice coefficient ranges from 0 (no spatial overlap) to 1 (perfect overlap) and characterizes the geometric agreement between predicted and MRI-derived tumor shapes. For Dice, NTA, and tumor boundary calculations, the tumor region was defined by thresholding the normalized tumor volume fraction at $\phi = 0.25$ for both MRI-derived fields and model predictions. A threshold sensitivity check for Rat III at Day 19 showed only modest changes across $\phi = 0.20$, 0.25, and 0.30, with NTA values of 0.27, 0.26, and 0.25 and Dice values of 0.91, 0.93, and 0.93, respectively. These small variations indicate that the reported predictive trends are not sensitive to moderate changes in the tumor volume fraction cutoff. Finite element simulations are performed using FEniCS (Alnæs et al. 2015), and both LA and gpCN Bayesian inference, including scalable evaluation of posterior model plausibility, are implemented using hIPPYLib (Villa et al. 2021, 2018, 2016).

3.1 Calibration parameters and hyper-parameter specification

Among the biophysical parameters defining the biomechanical tumor growth model (1) and (2), the calibration parameters are tumor diffusivity, proliferation rate, and elastic modulus $\boldsymbol{\theta} = (\log D(\boldsymbol{X}, t), \log G(\boldsymbol{X}, t), \log E(\boldsymbol{X}, t))$ that are considered as subject-specific, and spatially varying and represented in logarithmic to ensure their positive values within the sequential Bayesian inference. These fields are sequentially updated via Bayesian filtering using longitudinal MRI data, as they directly control tumor infiltration, volumetric growth, and growth-induced mechanical resistance. The stress-mediated diffusivity decay coefficient H, the growth–mechanics coupling coefficient C, and Poisson's ratio ν are treated as spatially homogeneous and fixed. The biophysical motivation of this choice is that C governs the magnitude of tumor-induced mass effect, whose spatial variation cannot be reliably inferred from imaging data alone, while H globally modulates stress-induced growth inhibition and together with ν are weakly identifiable given MRI data of tumor volume fraction. To assess whether this choice affects model selection, a sensitivity analysis with ±25% perturbations of C and H is reported in the *Supplementary Information*, indicating the posterior plausibility trends were preserved under these perturbations. Prior means and variances for the inferred parameters, along with values of the fixed parameters, are taken from spatially homogeneous posterior estimates reported for Wistar rat glioma growth (Lima et al. 2016; Hormuth et al. 2017, 2015) and are summarized in Table 1. The table also reports the prior correlation lengths ρ_E, ρ_D, and ρ_G, and the observation noise variance σ_{noise}, determined via the cross-validation procedure

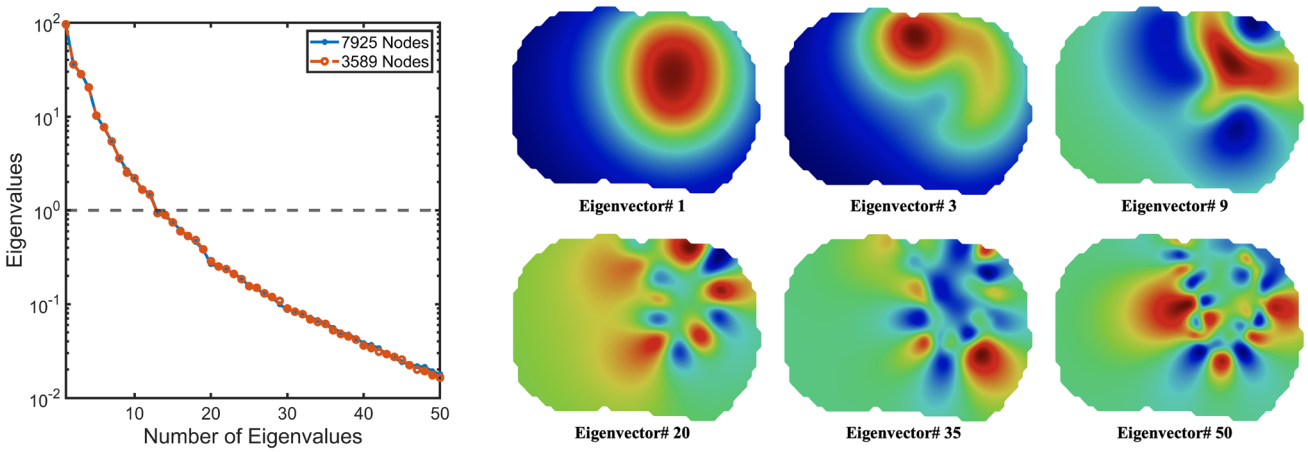


Fig. 1 Scalability of the LA solution of Bayesian inference for Rat III from MRI data of days 10-16. Eigenvalue decay and selected eigenvectors of the prior-preconditioned data misfit Hessian demonstrate rapid spectral decay, mesh independence, and spatial localization of data-informed modes. The leading 50 Hessian eigenmodes were retained in the low-rank posterior approximation, while a rank-sensitivity check is reported in the *Supplementary Information*

Table 1 Hyper-parameters and fixed biophysical parameters used in the sequential Bayesian inference for four Wistar rats

Prior mean and variance of inferred parameters			
	$\log(E)$	$\log(D)$	$\log(G)$
Units	log(kPa)	$\log(\text{mm}^2/\text{day})$	$\log(\text{day}^{-1})$
Mean	−0.1562	−0.3492	−1.8965
Variance	0.01	0.09	0.0064

Prior correlation lengths and noise variance				
	ρ_E (mm)	ρ_D (mm)	ρ_G (mm)	σ^2_{noise}
Value	5.5	6.5	3.5	1.23×10^{-3}

Fixed biophysical model parameters			
Parameter	H (kPa^{-1})	C (kPa)	ν (–)
Value	1.5	0.65	0.45

described in Liang et al. (2023). In particular, MRI data from Rat III over days 10–16 are used in a grid search, with Pareto-optimal hyper-parameters selected by maximizing Dice agreement and minimizing NTA prediction error at the final prediction time at day 19. These hyper-parameters are then fixed and applied to the remaining subjects.

3.2 Sequential Bayesian inference of biomechanical tumor growth model

Figure 1 demonstrates the scalability of the LA solution of the high-dimensional spatial inference in Rat III MRI. The rapid and mesh-independent decay of the prior-preconditioned data misfit Hessian spectrum indicates that the effective dimension of the inference problem is governed by the information content of the imaging data rather than mesh resolution. Leading eigenvectors localize in regions influenced by tumor growth, confirming that data primarily inform parameters in mechanically active domains. Based on the truncation error in spectral decay indicated in equation (S.5) of the *Supplementary Information*, the leading 50 Hessian eigenmodes were retained in the low-rank posterior approximation for all animals. A rank-sensitivity check using 60 modes is reported in the *Supplementary Information* and showed no change in posterior model plausibility to the reported precision (Table S2).

Figures 2, 3, 4 and 5 compare MRI-derived tumor volume fractions with sequential predictions obtained from the hyperelastic mechanically coupled tumor growth model (1) and (2), evaluated at the maximum a posteriori (MAP) parameters for four rats. For each subject, the model is sequentially informed by imaging data available up to a given time point and used to predict tumor evolution at the subsequent imaging time. We refer to this as *one-scan-ahead* prediction to the next, unseen MRI acquisition time. The results show that subject-specific Bayesian filter of spatially varying calibration parameters captures the overall anisotropic tumor spread and irregular growth patterns across animals. Prediction accuracy improves as additional scans are assimilated including subject-to-subject variability in predictive performance. A multi-step prediction experiment without intermediate data assimilation is reported in the *Supplementary Information* and shows the expected degradation of prediction accuracy over longer forecast horizons (Fig. S1).

Figure 6 shows the evolution of the MAP estimates of the spatially varying tumor diffusivity D, proliferation rate G, and elastic modulus E for Rat III during sequential Bayesian inference. As additional MRI data are assimilated, the inferred parameter fields retain coherent spatial structure while becoming progressively refined. These fields provide one estimate of the spatial heterogeneity, while the degree to which each parameter is informed by the data is assessed below using posterior uncertainty reduction. Moreover, the spatial correlation imposed by the priors enables information from the tumor region to propagate into the surrounding tissue, supporting inference of heterogeneous growth patterns and accurate prediction of the tumor shapes. In particular, the inferred elastic modulus E exhibits spatial contrast between the tumor region and adjacent tissue, with lower E in regions of high tumor burden. Through the constitutive relation defining the first Piola–Kirchhoff stress $\mathbf{P}$, this stiffness heterogeneity modulates the mechanical response in (2), thereby shaping the stress field that feeds back into tumor expansion via the stress-dependent diffusivity term in (1). The inferred diffusivity D exhibits spatial heterogeneity aligned with the observed directions of tumor spread, while the proliferation rate G remains more localized, with elevated values confined to the actively growing tumor region. The

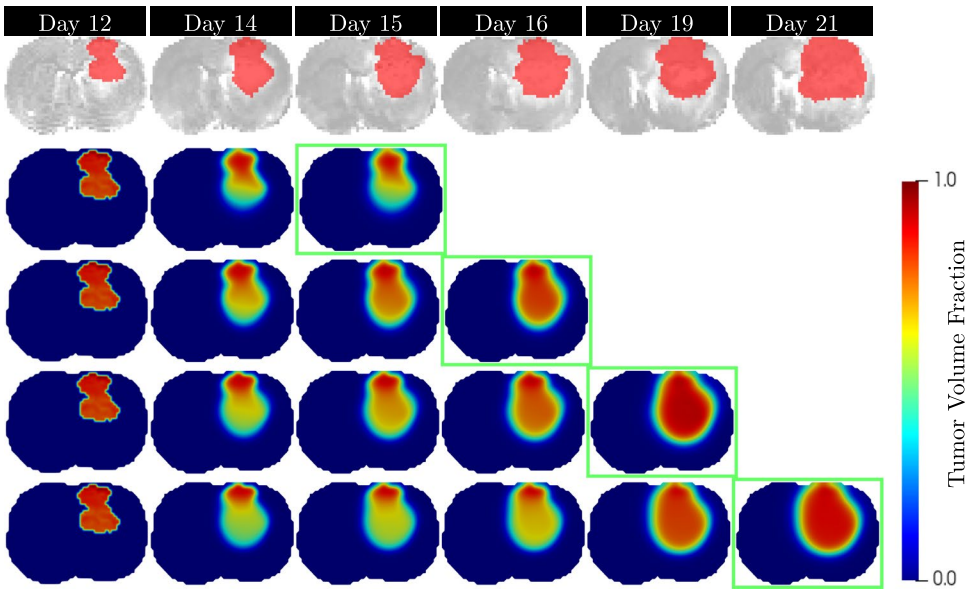


Fig. 2 Sequential one-scan-ahead prediction for Rat I at MAP parameters using the hyperelastic mechanically coupled tumor growth model defined in (1) and (2). Top row: MRI-derived tumor volume fraction. Bottom rows: model predictions obtained by assimilating data up to t_k and predicting the subsequent scan at t_{k+1} (boxed panels). Dice values between the predicted and MRI-derived tumor at Day 15, Day 16, Day 19 and Day 21 are 0.85, 0.91, 0.9, and 0.92 respectively

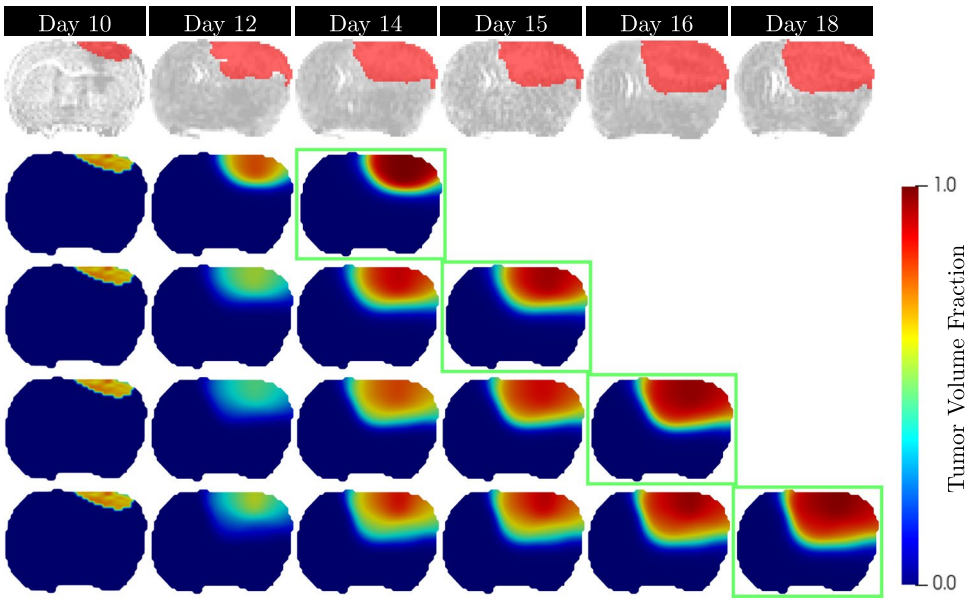


Fig. 3 Sequential one-scan-ahead prediction for Rat-II at MAP parameters using the hyperelastic mechanically coupled tumor growth model defined in (1) and (2). Top row: MRI-derived tumor volume fraction. Bottom rows: model predictions obtained by assimilating data up to t_k and predicting the subsequent scan at t_{k+1} (boxed panels). Dice values between the predicted and MRI-derived tumor at Day 14, Day 15, Day 16 and Day 18 are 0.88, 0.96, 0.95, and 0.95 respectively

inferred baseline diffusivity should not be interpreted as a pointwise map of invasion intensity at the apparent tumor boundary; in the reaction–diffusion model, invasion is governed by the diffusive flux, which depends on both D and the spatial gradient of ϕ, and in the mechanically coupled model also on stress-mediated modulation.

To assess the how much the MRI data informs the inferred spatial parameter fields, we quantified the reduction of posterior uncertainty relative to the prior. For each inferred parameter field $\theta \in \log D, \log G, \log E$, we computed the local posterior uncertainty reduction index,

$$\mathcal{R}_\theta = 1 - \frac{\sqrt{\mathrm{Var}_{\pi_{\mathrm{post}}}(\theta)}}{\sqrt{\mathrm{Var}_{\pi_{\mathrm{pr}}}(\theta)}}. \tag{16}$$

Here, $\mathcal{R}_\theta$ close to zero indicates small local reduction in uncertainty relative to the prior, whereas larger values indicate regions where the MRI data more strongly constrain the parameter field. The resulting maps for Rat III at Day 19 are shown in Fig. 7. The uncertainty reduction is concentrated in the tumor-bearing and peritumoral regions, with stronger reduction for diffusivity and proliferation than for stiffness. This trend is expected because D and G directly

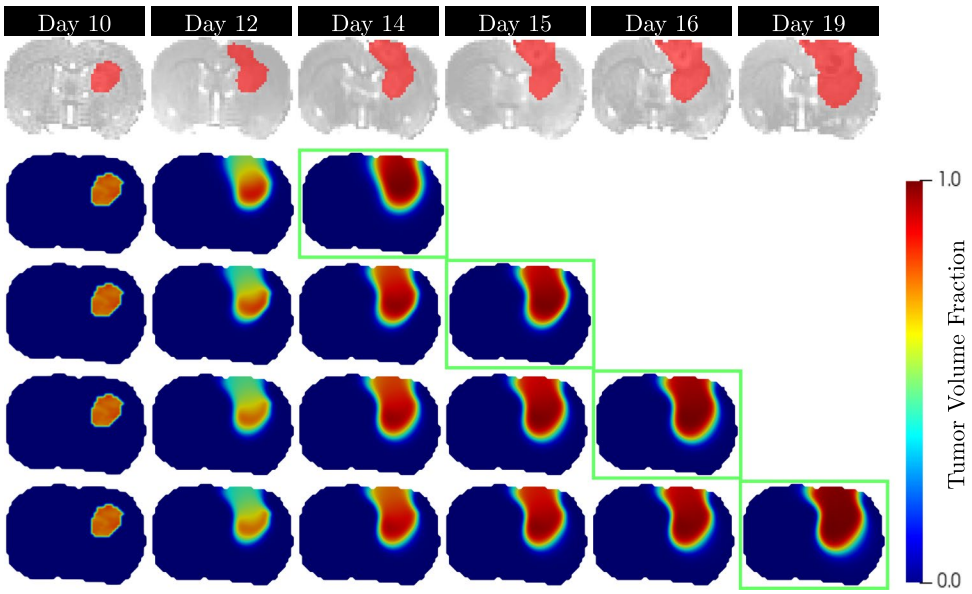


Fig. 4 Sequential one-scan-ahead prediction for Rat-III at MAP parameters using the hyperelastic mechanically coupled tumor growth model defined in (1) and (2). Top row: MRI-derived tumor volume fraction. Bottom rows: model predictions obtained by assimilating data up to t_k and predicting the subsequent scan at t_{k+1} (boxed panels). Dice values between the predicted and MRI-derived tumor at Day 14, Day 15, Day 16 and Day 19 are 0.86, 0.9, 0.82, and 0.92 respectively

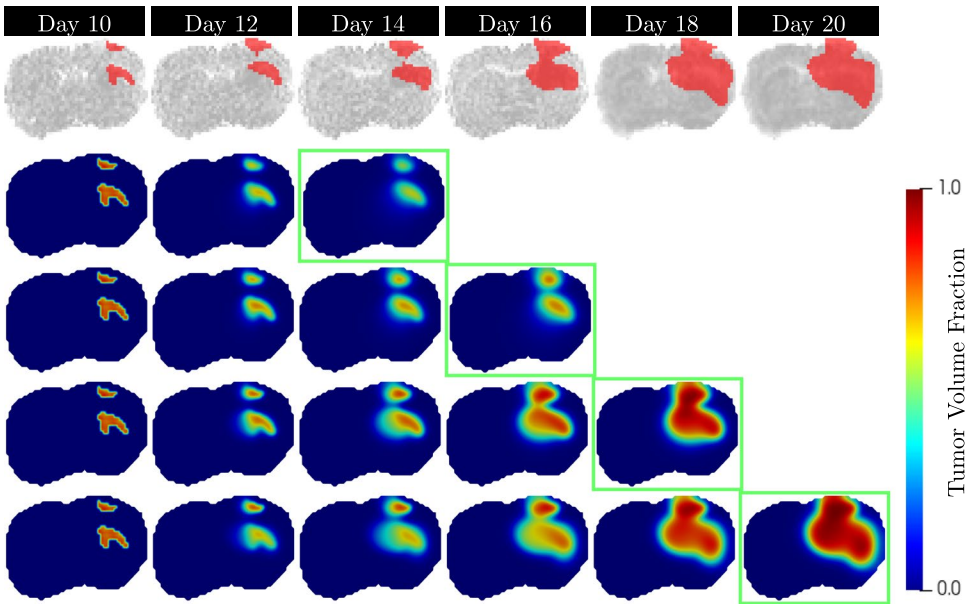


Fig. 5 Sequential one-scan-ahead prediction for Rat IV at MAP parameters using the hyperelastic mechanically coupled tumor growth model defined in (1) and (2). Top row: MRI-derived tumor volume fraction. Bottom rows: model predictions obtained by assimilating data up to t_k and predicting the subsequent scan at t_{k+1} (boxed panels). Dice values between the predicted and MRI-derived tumor at Day 14, Day 16, Day 18, and Day 20 are 0.72, 0.71, 0.85, and 0.89 respectively

control tumor volume fraction evolution, whereas E affects the observed tumor volume fraction only indirectly through the mechanical coupling.

Figures 8, 9 and 10 compare the low-rank LA with the sampling-based gpCN algorithm for Rat III to assess the accuracy of the LA posterior approximation. The gpCN sampler is used here as an independent sampling-based reference rather than as an exact ground truth, since both approaches approximate the same Bayesian posterior using different computational strategies. As discussed in *Supplementary Information*, both methods are applicable to high-dimensional parameter spaces, although gpCN is substantially more computationally demanding because it requires many posterior samples and repeated finite element solves. In this study, gpCN was run using four chains of length 5000, with each chain requiring approximately 56.4 h of computation, whereas the corresponding LA solution required about 4 h on the same processor. Figure 8 compares LA and gpCN estimates of the marginal posterior distributions of inference parameters at two locations within the tumor in Rat III, using MRI data from Day 10 to Day 16. Overall, LA provides a reasonable approximation of the local posterior, with the best agreement observed for $\log(G)$ and $\log(E)$ and the largest discrepancy occurring for $\log(D)$. As an additional sampling-based validation of the LA model evidence approximation, (S.14) in the *Supplementary Information*, we

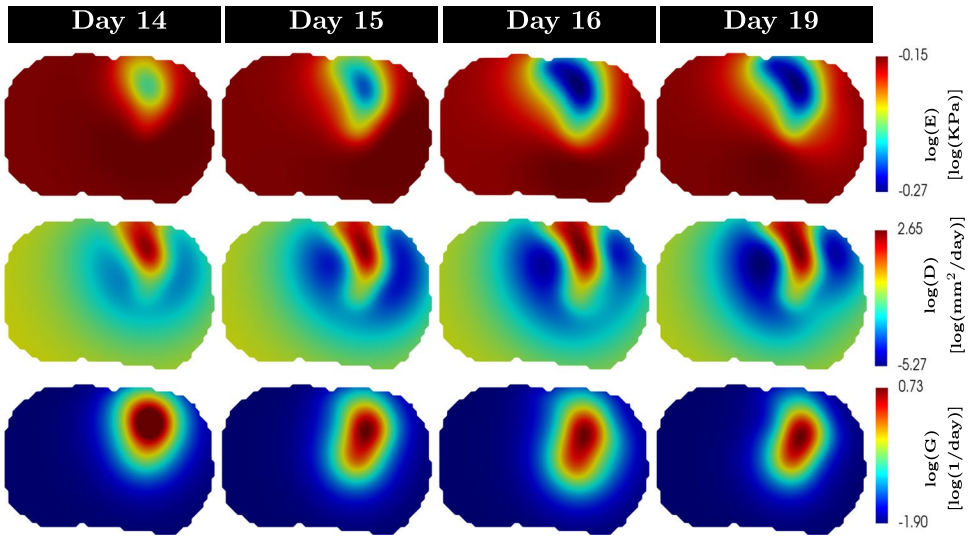


Fig. 6 Evolution of MAP estimates of spatially varying elastic modulus $E(\mathbf{X})$, tumor diffusivity $D(\mathbf{X})$, and proliferation rate $G(\mathbf{X})$ for Rat-III during sequential Bayesian inference

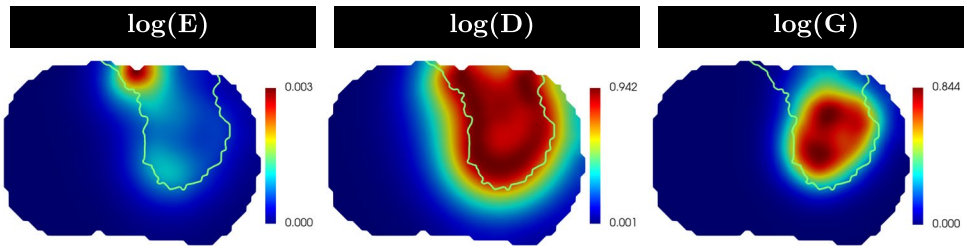


Fig. 7 Spatial maps of the local posterior uncertainty reduction index $\mathcal{R}_\theta$ for the inferred parameter fields for Rat III on Day 19 including the overlay of the model-predicted tumor boundary. Higher values correspond to regions where the longitudinal MRI data provide stronger local constraints on the parameter field, while lower values indicate regions that remain weakly informed by the data

also estimated the relative model plausibility from the gpCN posterior samples for Rat III at Day 19. This comparison was restricted to the two mechanically coupled formulations and therefore the reported plausibility values were normalized over the linear elastic and hyperelastic coupled reaction–diffusion models (see Sect. 3.3 for more details). The LA and gpCN estimates yielded nearly identical plausibility values, preserving the same model ranking. When normalized over the two mechanically coupled formulations, both approaches assigned approximately 49% plausibility to the linear elastic model and 51% plausibility to the hyperelastic model. This agreement indicates that the low-rank LA evidence approximation provides a reliable estimate of relative model plausibility for the dynamic model-selection framework.

Figure 9 compares MRI-derived tumor boundaries with the MAP prediction and boundary ensembles generated from posterior samples obtained by LA and gpCN. The two methods produce tumor boundary envelopes of similar width at both Day 16 and Day 19, indicating comparable uncertainty in the predicted tumor morphology. Figure 10 compares the displacement and stress fields at the MAP estimate and across posterior samples for the Day 19 prediction. While LA and gpCN produce qualitatively consistent spatial patterns, gpCN samples exhibit slightly smaller displacement and stress magnitudes. This difference is consistent with the diffusivity discrepancies observed in Fig. 8, consistent with the slightly larger posterior diffusivity inferred by gpCN.

Overall, these comparisons show that LA reproduces the main characteristics of the sampling-based posterior relevant to this study, including marginal parameter distributions, tumor-boundary uncertainty, mechanically induced displacement and stress patterns, and relative model plausibility. Although modest differences remain, particularly in the posterior of $\log(D)$, these differences do not alter the predicted tumor morphology or the qualitative ordering of competing biomechanical models. Owing to its substantially lower computational cost, LA is adopted in the remainder of this work for sequential Bayesian inference and dynamic model selection.

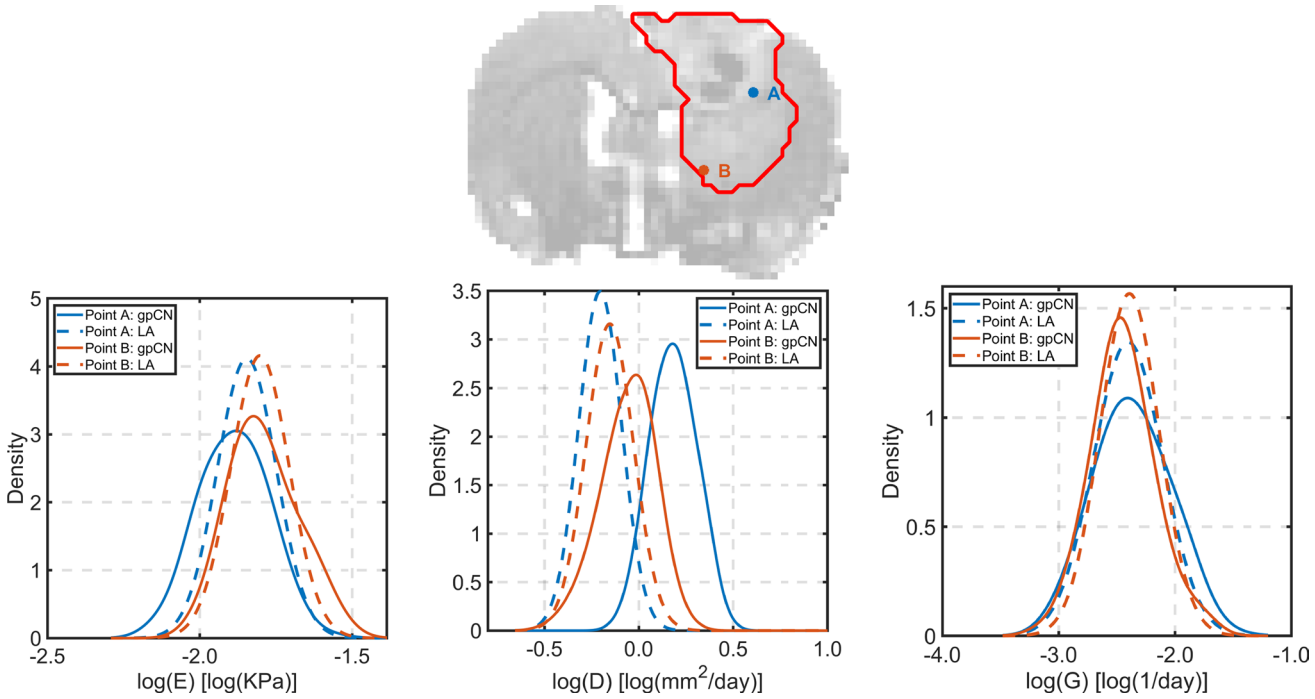


Fig. 8 Comparison of LA and gpCN posterior estimates: point-wise kernel density estimates (KDEs) of inference parameters at two locations within the tumor in Rat III

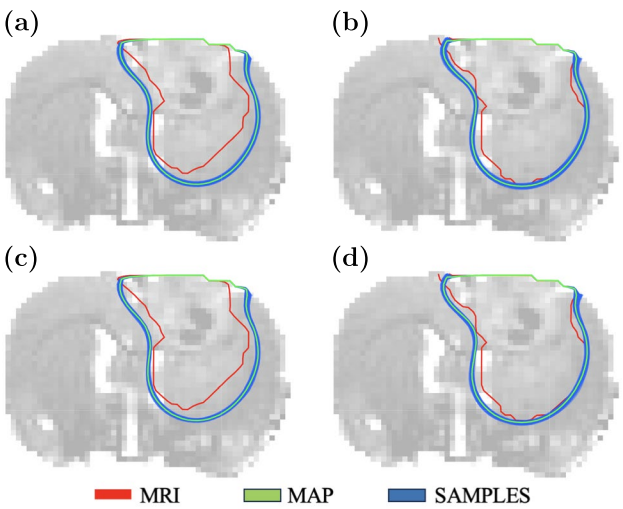


Fig. 9 Comparison of tumor boundary predictions from LA and gpCN posterior samples (blue) with MRI-derived boundaries (red) and MAP predictions (green) in Rat III: (a,b) LA samples and (c,d) gpCN samples. Panels (a,c) correspond to Day 16 and (b,d) to Day 19 predictions. A total of 1000 samples are used for each method

3.3 Dynamic selection of biomechanical tumor models

While spatially varying parameter inference captures heterogeneity in tumor growth and tissue mechanics within a prescribed model, it does not by itself determine whether the assumed biomechanical formulation remains the most plausible description as additional MRI data are acquired. Glioma growth is a dynamic process in which the relative importance of diffusion, proliferation, mass effect, and stress-mediated feedback may evolve as the tumor expands within the confined brain. Therefore, rather than assuming a single fixed mechanical formulation a priori, we evaluate competing biomechanical models sequentially for each animal. At each assimilation time, the candidate models are recalibrated using the accumulated MRI data from that subject, their posterior model plausibilities are recomputed, and the resulting model ranking can be used to select the formulation for subject-specific one-scan-ahead prediction. To this end, *dynamic selection* refers to time-updated, subject-specific posterior model comparison, not automatic discovery of new model equations.

In this work, we demonstrate this approach by comparing three competing tumor growth models: a reaction-diffusion model with hyperelastic mechanics (*RD+Hyperelastic*) as detailed in Sect. 2.2, a reaction-diffusion model with linear elastic mechanics (*RD+Linearelastic*), and a reaction-diffusion model without mechanical deformation (*RD*). For the *RD+Linearelastic* model, the governing equations (1)–(2) are simplified by assuming infinitesimal deformations. Under this assumption, growth-induced volume change is neglected and the first Piola–Kirchhoff stress in (4) is replaced by the linear elastic stress, parameterized by the elastic modulus E and Poisson's ratio ν,

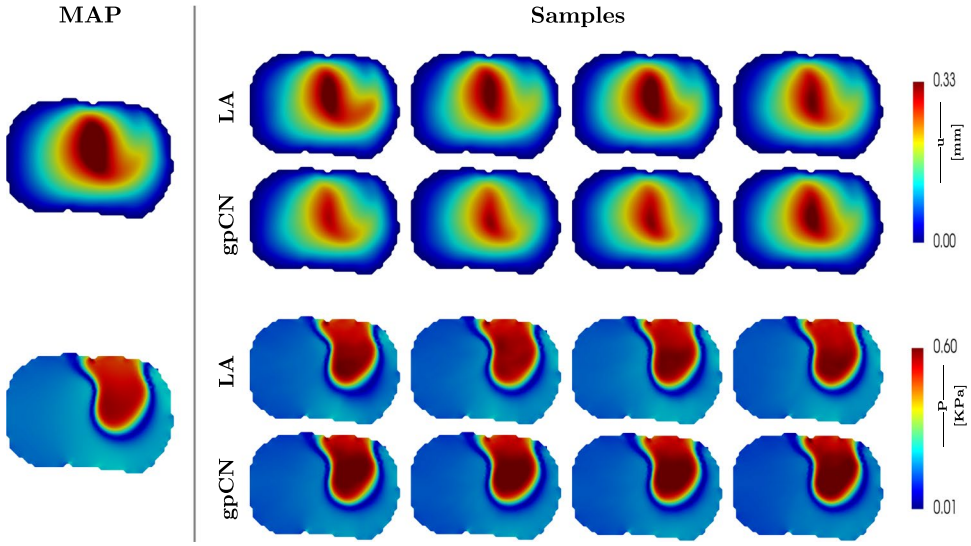


Fig. 10 Comparison of displacement and stress fields for Rat III: MAP estimates and posterior samples obtained from LA and gpCN for the Day 19 prediction

$$\begin{aligned} \boldsymbol{P} &= \frac{E}{(1+\nu)(1-2\nu)}[\nu\,\mathrm{tr}(\boldsymbol{\epsilon})\,\mathbf{I} + (1-2\nu)\boldsymbol{\epsilon}], \\ \boldsymbol{\epsilon} &= \frac{1}{2}\left(\nabla\mathbf{u} + \nabla\mathbf{u}^T\right), \end{aligned} \tag{17}$$

where $\boldsymbol{\epsilon}$ is the strain tensor. In the small-strain limit, the first Piola–Kirchhoff stress is equivalent to the Cauchy stress, and distinctions between reference and deformed configurations are neglected. The *RD* model omits mechanical coupling by removing the mechanical PDE (2) and setting the stress-dependent term $e^{-Hp_\tau} = 1$ in (1).

Figure 11 summarize the subject-specific dynamic model selection results for the four rats by tracking posterior model plausibility together with one-scan-ahead predictive Dice. For each animal, posterior plausibility is recomputed at each assimilation time using the MRI data accumulated for that animal up to that point. The NTA panel reports the prediction obtained from the model with the highest posterior plausibility at each assimilation time, rather than a fixed model used throughout the full time series. Thus, the NTA trajectory represents the dynamically selected subject-specific prediction, with the selected model switching between *RD+Linearelastic* and *RD+Hyperelastic* at some intermediate imaging times. The *RD* model is generally the least plausible, particularly at later imaging times, indicating that diffusion–proliferation alone is less supported by the longitudinal data than mechanically coupled formulation. Thus, within the present murine dataset, the inclusion of mechanical coupling through mass effect and stress-mediated feedback, results in more plausible computational models. Across rats, the competition is primarily between *RD+Linearelastic* and *RD+Hyperelastic*. The posterior model plausibility for these two mechanically coupled models evolves with the available MRI data and varies by subject, with the hyperelastic formulation often becoming more plausible at later imaging times. This trend is consistent with increasing relevance of finite-deformation mechanics as tumor burden and growth-induced deformation increase. Importantly, the Dice and NTA trends in this figure do not reliably discriminate between *RD+Linearelastic* and *RD+Hyperelastic*, because these metrics primarily measure tumor shape agreement and are only weakly sensitive to the underlying mechanical state. Posterior model plausibility therefore provides a complementary, more mechanistically meaningful criterion for comparing whether each formulation consistently explains the observed spatiotemporal tumor evolution under its own biomechanical assumptions.

To directly connect model plausibility to biomechanics, Figs. 12, 13 and 14 compare the *RD+Linearelastic* and *RD+Hyperelastic* predictions and inferred parameter fields for Rat I. Although the predicted tumor volume fraction fields ϕ are visually similar between the two models, the displacement and stress fields differ and diverge further at later times (Fig. 12), when *RD+Hyperelastic* receives higher posterior plausibility (Fig. 11). This demonstrates that comparable tumor shape agreement does not imply comparable biomechanics: constitutive assumptions can produce similar tumor morphology while inducing substantially different mechanical states. The quantitative comparison in Fig. 13 supports this interpretation that NTA evolves similarly for the two models, whereas the domain-averaged displacement and stress magnitudes show larger differences over time.

The inferred parameter evolution clarifies the mechanical origin of the model preference. While the growth kinetics parameters $\log(D)$ and $\log(G)$ remain similar between *RD+Linearelastic* and *RD+Hyperelastic*, the stiffness field

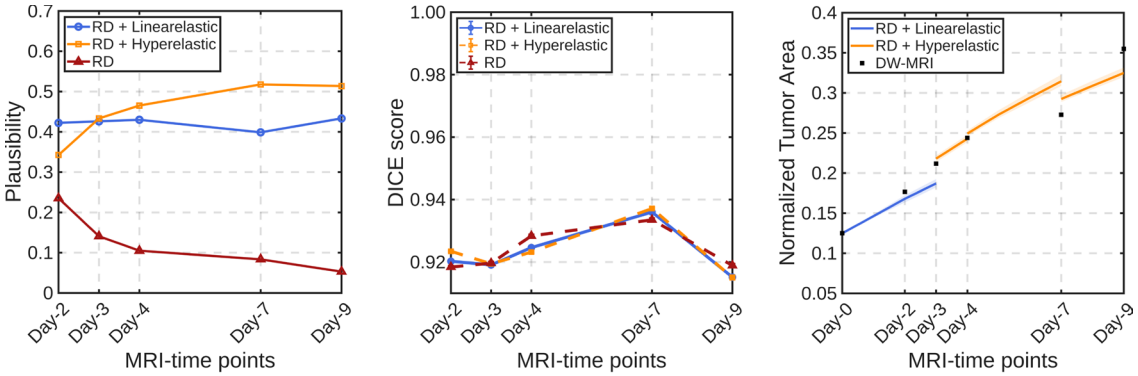
$\log(E)$ differs markedly (Figure 14). Under the small-strain linear elastic assumption, $\log(E)$ progressively shifts toward a broadly softened state across the domain. This pattern suggests that, as mass effect increases, the linear elastic model compensates for missing finite deformation kinematics by reducing the inferred stiffness to match the observed tumor expansion. In contrast, the hyperelastic formulation accommodates finite strain kinematics directly and yields a more spatially localized stiffness pattern near the tumor. Thus, although both models can produce similar tumor morphology, their inferred stiffness fields and mechanical responses are not equivalent. This helps explain why posterior plausibility can favor the hyperelastic formulation even when Dice and NTA differences are small, as the evidence reflects biomechanical consistency, not merely agreement of tumor shape.

Overall, the dynamic model selection results show that, in the present longitudinal murine dataset, mechanically coupled formulations are favored over the uncoupled reaction-diffusion tumor growth model, and the relative support for linear elastic versus hyperelastic mechanics evolves across subjects and imaging times. These findings motivate the use of posterior model plausibility, together with morphology-based metrics, as a subject-specific criterion for evaluating biomechanical model adequacy in MRI-driven computational tumor growth prediction.

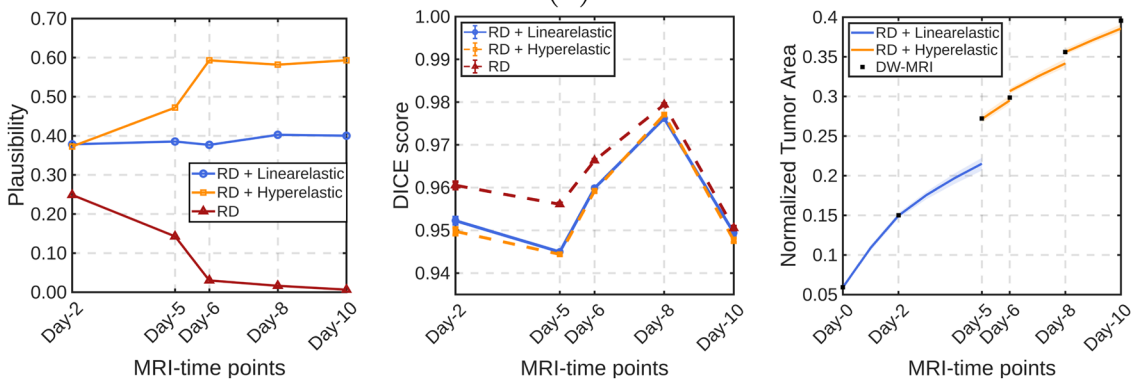
4 Discussion and conclusions

In this study, we developed an MRI-driven framework for sequential Bayesian inference of biomechanical tumor growth models within a high-dimensional spatial parameterization. Longitudinal imaging data of murine models of glioma were assimilated to update subject-specific fields of diffusivity, proliferation rate, and elastic modulus within a spatially varying parameter space. To investigate the role of mechanics in tumor evolution, we compared three competing tumor growth models: a reaction–diffusion model without mechanical coupling, a reaction–diffusion model coupled with linear elasticity, and a reaction–diffusion model coupled with hyperelastic mechanics. Posterior model plausibility, based on model evidence, was evaluated sequentially as new MRI data were incorporated, enabling subject-specific dynamic selection of the most plausible candidate model for one-scan-ahead prediction at each assimilation time. The results show that, within the present longitudinal murine dataset, mechanically coupled models were generally more plausible than the uncoupled RD model. This finding is consistent with prior evidence that solid stresses generated by tumor expansion under tissue confinement can regulate proliferation, apoptosis, and invasion through mechanobiological pathways (Helmlinger et al. 1997; Stylianopoulos et al. 2013; Jain et al. 2014; Faghihi et al. 2020). The posterior plausibility trends indicate that diffusion–proliferation alone is less supported by the MRI time series than formulations that include mass effect and growth–stress feedback. Among the mechanically coupled models, the relative support for linear elastic and hyperelastic mechanics evolved across subjects and imaging times, with the hyperelastic formulation often favored at later scans when tumor burden and deformation were larger. This trend suggests that finite-deformation effects can become important during progression, while linear elasticity may remain competitive when deformation is modest. Importantly, Dice score and NTA often did not distinguish between the two mechanically coupled models, even when their displacement, stress, and inferred stiffness fields differed. Thus, posterior model plausibility provides a mechanics-informed complement to morphology-based metrics for evaluating biomechanical model adequacy.

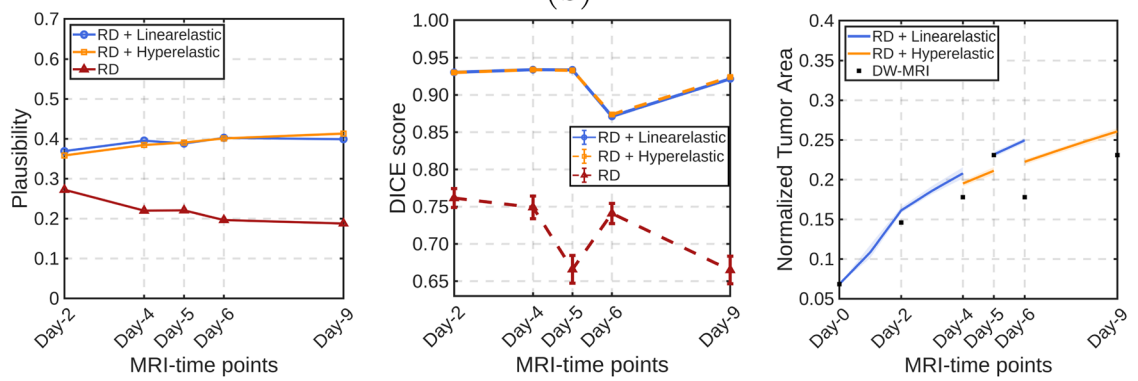
This study has several limitations. First, although consistent trends were observed across the analyzed animals, the cohort remains small, and larger longitudinal studies are needed before drawing population level conclusions about identified mechanical regimes. Second, the present analysis was conducted in a two dimensional (2D) based on MRI slices to enable repeated high-dimensional Bayesian inference, gpCN comparison, and model evidence evaluation across competing PDE models. The slice-selection and adjacent slice analyses reported in the *Supplementary Information* support the robustness of the main trends, but fully three dimensional (3D) Bayesian model selection remains an important extension. To this end, reliable reduced-order or neural-operator surrogate models may help make such studies computationally feasible while preserving biomechanical fidelity (Singh et al. 2024; Islam et al. 2025). Third, the tumor model is intentionally parsimonious and does not explicitly include necrosis, apoptosis, or additional cellular compartments. Extending the framework to richer multiphase tumor-growth models (Faghihi et al. 2020; Lucci et al. 2022) and biology-informed hyperelastic constitutive laws (Goriely et al. 2015) will require additional imaging biomarkers or histological data to avoid introducing poorly identifiable states. Fourth, not all biophysical parameters can be reliably inferred as spatially varying from MRI-derived tumor volume fraction alone. Mechanical quantities are only indirectly observed through model coupling, and the fixed parameters C, H, and ν were therefore prescribed rather than inferred. Sensitivity analyses for C and H are provided in the *Supplementary Information* showed that the main model-plausibility trends were preserved. Future work


Plausibility
RD + Linearelastic
RD + Hyperelastic
RD
Day-2
Day-3
Day-4
Day-7
Day-9
MRI-time points
DICE score
RD + Linearelastic
RD + Hyperelastic
RD
Day-2
Day-3
Day-4
Day-7
Day-9
MRI-time points
Normalized Tumor Area
RD + Linearelastic
RD + Hyperelastic
DW-MRI
Day-0
Day-2
Day-3
Day-4
Day-7
Day-9
MRI-time points

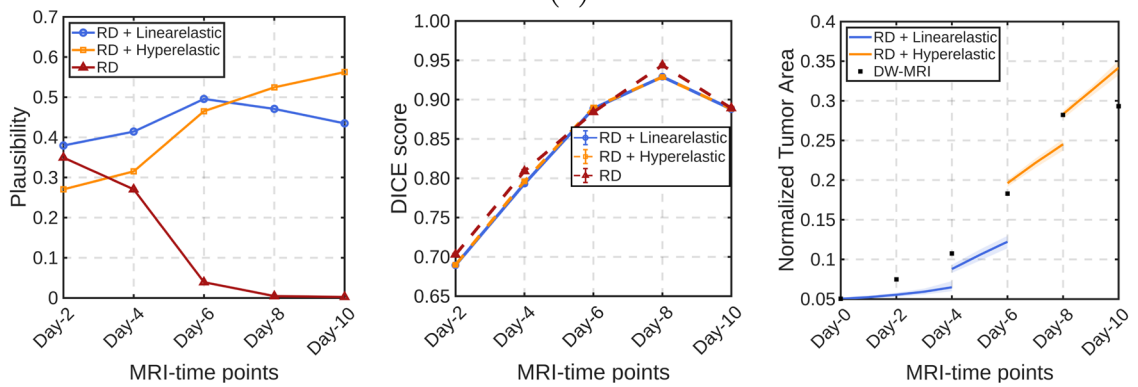
(a)


Plausibility
RD + Linearelastic
RD + Hyperelastic
RD
Day-2
Day-5
Day-6
Day-8
Day-10
MRI-time points
DICE score
RD + Linearelastic
RD + Hyperelastic
RD
Day-2
Day-5
Day-6
Day-8
Day-10
MRI-time points
Normalized Tumor Area
RD + Linearelastic
RD + Hyperelastic
DW-MRI
Day-0
Day-2
Day-5
Day-6
Day-8
Day-10
MRI-time points

(b)


Plausibility
RD + Linearelastic
RD + Hyperelastic
RD
Day-2
Day-4
Day-5
Day-6
Day-9
MRI-time points
DICE score
RD + Linearelastic
RD + Hyperelastic
RD
Day-2
Day-4
Day-5
Day-6
Day-9
MRI-time points
Normalized Tumor Area
RD + Linearelastic
RD + Hyperelastic
DW-MRI
Day-0
Day-2
Day-4
Day-5
Day-6
Day-9
MRI-time points

(c)


Plausibility
RD + Linearelastic
RD + Hyperelastic
RD
Day-2
Day-4
Day-6
Day-8
Day-10
MRI-time points
DICE score
RD + Linearelastic
RD + Hyperelastic
RD
Day-2
Day-4
Day-6
Day-8
Day-10
MRI-time points
Normalized Tumor Area
RD + Linearelastic
RD + Hyperelastic
DW-MRI
Day-0
Day-2
Day-4
Day-6
Day-8
Day-10
MRI-time points

(d)

◂**Fig. 11** Temporal evolution of posterior model plausibility, one-scan-ahead predictive Dice score, and normalized tumor area (NTA) in (a) Rat I, (b) Rat II, (c) Rat III, and (d) Rat IV. Posterior plausibility is shown for the three candidate models: reaction–diffusion without mechanics (*RD*), reaction–diffusion coupled to linear elasticity (*RD+Linearelastic*), and reaction–diffusion coupled to hyperelastic mechanics (*RD+Hyperelastic*). The NTA panel shows the prediction from the most plausible model at each assimilation time, for each subject. Error bars in Dice and shaded bounds in NTA denote 95% credible intervals propagated from the posterior parameter distributions

should incorporate MRI-derived estimates of mass effect and deformation, as in Tunç et al. (2021), to more directly constrain displacement and stress fields and should explicitly propagate segmentation, registration, and ADC-processing uncertainty. Finally, the conclusions regarding mechanical coupling and constitutive plausibility are restricted to the observed 10–21 day progression window, and extrapolation beyond this period will require additional longitudinal imaging data.

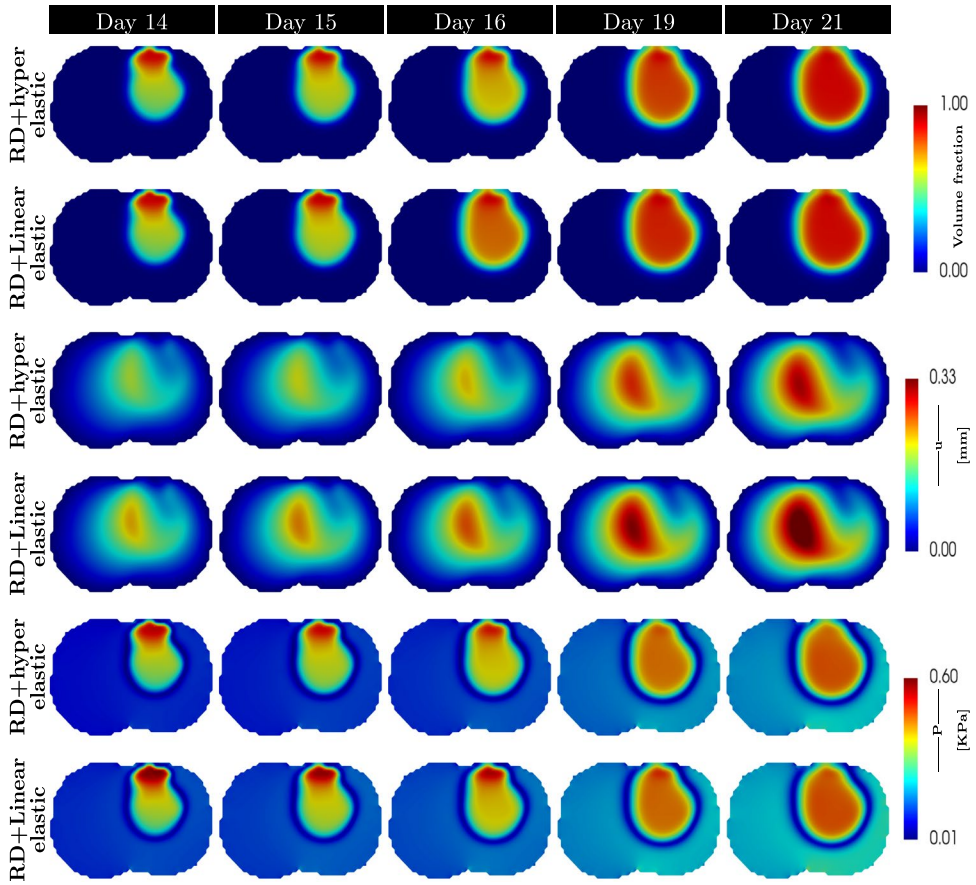


Fig. 12 Comparison of one-scan-ahead predictions for Rat-I under *RD+Hyperelastic* and *RD+Linearelastic* formulations. Tumor volume fraction $\phi(\mathbf{X})$, displacement magnitude $\|\mathbf{u}(\mathbf{X})\|$, and first Piola–Kirchhoff stress magnitude $\|\mathbf{P}(\mathbf{X})\|$ are shown at sequential imaging times

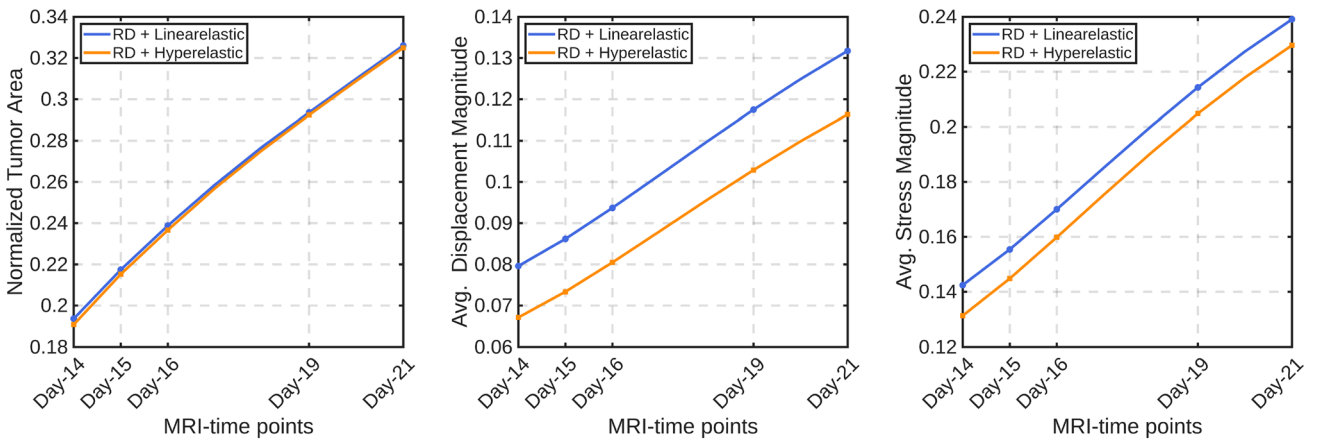


Fig. 13 Comparison of *RD+Hyperelastic* and *RD+Linearelastic* predictions for Rat I in terms of normalized tumor area (NTA), domain-averaged displacement magnitude, and domain-averaged first Piola–Kirchhoff stress magnitude over time

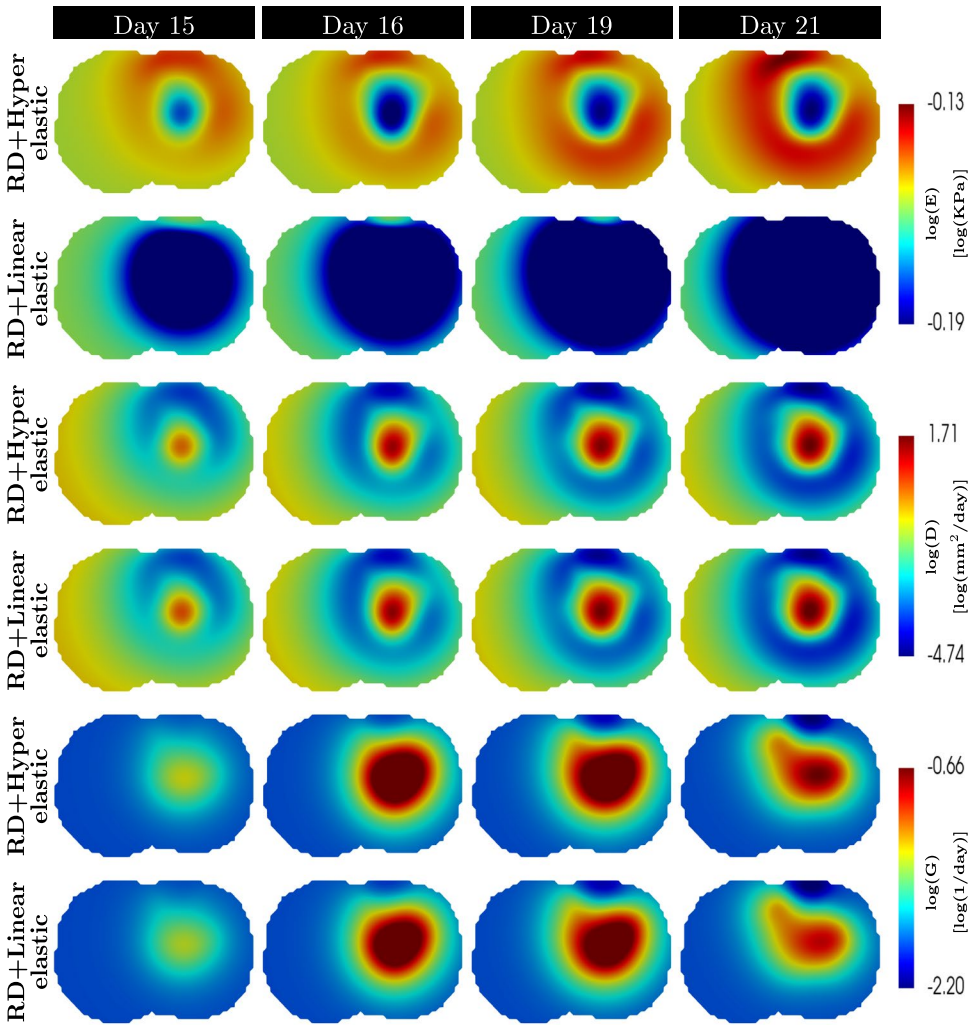


Fig. 14 Evolution of MAP estimates of spatially varying elastic modulus $E(\mathbf{X})$, tumor diffusivity $D(\mathbf{X})$, and proliferation rate $G(\mathbf{X})$ for Rat I under *RD+Hyperelastic* and *RD+Linearelastic* models

The proposed sequential inference and model-selection framework provides a natural foundation for patient-specific biomechanical cancer digital twins, in the spirit of recent efforts (Chaudhuri et al. 2023; Pash et al. 2026; Kapteyn et al. 2026). In such a setting, clinical MRI scans would be assimilated over time to update not only model parameters, but also the plausibility of competing growth, treatment response, or post surgical progression models. This is particularly important under therapy, where adaptive treatment decisions can alter the observed tumor dynamics. One-scan-ahead prediction as demonstrated in this work would provide a clinically relevant short horizon forecast before the next imaging or treatment decision, while dynamic model selection allows the prediction model to adapt to the subject specific response under different treatment regimes. Coupled with risk-averse optimization methods developed in our prior work (Tan and Faghihi 2024; Singh and Faghihi 2025), this framework could support patient specific "what if" simulations that balance tumor control against treatment induced toxicity. Realizing this goal will require prospective clinical validation and computational acceleration, for example through credible surrogate modeling strategies (Singh et al. 2024), because repeated Bayesian inference and model evidence evaluation across multiple PDE models may be too costly for clinical decision timelines.

In summary, this work introduces an MRI-informed framework for sequential, subject-specific evaluation of biomechanical tumor growth models. In the present murine glioma dataset, mechanically coupled formulations were favored over the uncoupled RD model, while the relative support for linear elastic versus hyperelastic mechanics changed across animals and imaging times as new scans were assimilated. These findings show the value of updating both spatial parameter fields and model plausibility from longitudinal imaging data, rather than prescribing a single biomechanical formulation a priori.

Supplementary Information The online version contains supplementary material available at https://doi.org/10.1007/s10237-026-02121-2.

Acknowledgements A.A.N. was partially supported by the State University of New York (SUNY) System Administration under SUNY Research Seed Grant Award No. 1191358. P.K.S. and D.F. acknowledge support from the U.S. National Science Foundation (NSF) through CAREER Award CMMI-2143662. D.A.H. acknowledge support from the NSF through the award DMS-2436499. The authors gratefully acknowledge computational support provided by the Center for Computational Research at the University at Buffalo.

Author contributions A.A.N. implemented the computational framework, performed the simulations, generated the results, and wrote the results section of the manuscript. P.K.S. contributed to code development and verification of the numerical implementation. D.A.H. provided the MRI data and contributed to the interpretation of the results. D.F. conceived the research, supervised the study, and wrote the rest of the manuscript.

Data availability The data supporting the findings of this study are available from the corresponding author upon reasonable request. The computational code used in this study is available at https://github.com/PCELab/RecursiveGliomaInference.

Declarations

Conflict of interest The authors declare that they have no conflict of interest.

Ethics approval All procedures involving animals were approved by the appropriate Institutional Animal Care and Use Committee (IACUC) at University of Texas at Austin and were performed in accordance with institutional guidelines and applicable national regulations for the care and use of laboratory animals.

Consent to participate Not applicable.

Open Access This article is licensed under a Creative Commons Attribution 4.0 International License, which permits use, sharing, adaptation, distribution and reproduction in any medium or format, as long as you give appropriate credit to the original author(s) and the source, provide a link to the Creative Commons licence, and indicate if changes were made. The images or other third party material in this article are included in the article's Creative Commons licence, unless indicated otherwise in a credit line to the material. If material is not included in the article's Creative Commons licence and your intended use is not permitted by statutory regulation or exceeds the permitted use, you will need to obtain permission directly from the copyright holder. To view a copy of this licence, visit http://creativecommons.org/licenses/by/4.0/.

References

Alghamdi A, Hesse MA, Chen J, Villa U, Ghattas O (2021) Bayesian poroelastic aquifer characterization from insar surface deformation data. 2. quantifying the uncertainty. Water Resour Res 57(11):e2021WR029775

Alnæs M, Blechta J, Hake J, Johansson A, Kehlet B, Logg A, Richardson C, Ring J, Rognes ME, Wells GN (2015) The fenics project version 1.5, Archive of numerical software 3 (100)

Anderson A, Xie J, Pizzonia J, Bronen R, Spencer D, Gore J (2000) Effects of cell volume fraction changes on apparent diffusion in human cells. Magn Reson Imaging 18(6):689–695

Atuegwu NC, Arlinghaus LR, Li X, Welch EB, Chakravarthy BA, Gore JC, Yankeelov TE (2011) Integration of diffusion-weighted mri data and a simple mathematical model to predict breast tumor cellularity during neoadjuvant chemotherapy. Magn Reson Med 66(6):1689–1696

Barnes SL, Sorace AG, Loveless ME, Whisenant JG, Yankeelov TE (2015) Correlation of tumor characteristics derived from DCE-MRI and DW-MRI with histology in murine models of breast cancer. NMR Biomed 28(10):1345–1356. https://doi.org/10.1002/nbm.3377

Budday S, Steinmann P, Kuhl E (2015) Physical biology of human brain development. Front Cell Neurosci 9:257

Chaudhuri A, Pash G, Hormuth DA, Lorenzo G, Kapteyn M, Wu C, Lima EA, Yankeelov TE, Willcox K (2023) Predictive digital twin for optimizing patient-specific radiotherapy regimens under uncertainty in high-grade gliomas. Front Artif Intell 6:1222612

Cotter SL, Roberts GO, Stuart AM, White D (2013) Mcmc methods for functions: modifying old algorithms to make them faster. Stat Sci 424–446

Daon Y, Stadler G (2016) Mitigating the influence of the boundary on pde-based covariance operators.arXiv:1610.05280 arXiv preprint

Faghihi D, Feng X, Lima EA, Oden JT, Yankeelov TE (2020) A coupled mass transport and deformation theory of multi-constituent tumor growth. J Mech Phys Solids 139:103936

Ghahramani M, Bavi O (2026) Biomechanical modeling of glioblastoma progression: a comprehensive review from classic mathematical frameworks to data-driven strategies: M. ghahramani and o. bavi, Biomechanics and Modeling in Mechanobiology 25 (1) 1

Goriely A, Geers MG, Holzapfel GA, Jayamohan J, Jérusalem A, Sivaloganathan S, Squier W, van Dommelen JA, Waters S, Kuhl E (2015) Mechanics of the brain: perspectives, challenges, and opportunities. Biomech Model Mechanobiol 14(5):931–965

Helmlinger G, Netti PA, Lichtenbeld HC, Melder RJ, Jain RK (1997) Solid stress inhibits the growth of multicellular tumor spheroids. Nat Biotechnol 15(8):778–783

Hogea C, Davatzikos C, Biros G (2007) Modeling glioma growth and mass effect in 3d mr images of the brain, in: International Conference on Medical Image Computing and Computer-Assisted Intervention, Springer, pp. 642–650

Hormuth DA II, Skinner JT, Does MD, Yankeelov TE (2014) A comparison of individual and population-derived vascular input functions for quantitative DCE-MRI in rats. Magn Reson Imaging 32(4):397–401

Hormuth DA II, Weis JA, Barnes SL, Miga MI, Rericha EC, Quaranta V, Yankeelov TE (2015) Predicting in vivo glioma growth with the reaction diffusion equation constrained by quantitative magnetic resonance imaging data. Phys Biol 12(4):046006

Hormuth DA, Weis JA, Barnes SL, Miga MI, Rericha EC, Quaranta V, Yankeelov TE (2017) A mechanically coupled reaction-diffusion model that incorporates intra-tumoural heterogeneity to predict in vivo glioma growth. J R Soc Interface 14(128):20161010

Hormuth DA, Weis JA, Barnes SL, Miga MI, Rericha EC, Quaranta V, Yankeelov TE (2017) A mechanically coupled reaction-diffusion model that incorporates intra-tumoural heterogeneity to predict in vivo glioma growth. J R Soc Interface 14(128):20161010

Hormuth DAI (2016) Predicting the spatio-temporal evolution of tumor growth and treatment response in a murine model of glioma. Vanderbilt University,(Ph.D. thesis)

Isaac T, Petra N, Stadler G, Ghattas O (2015) Scalable and efficient algorithms for the propagation of uncertainty from data through inference to prediction for large-scale problems, with application to flow of the antarctic ice sheet. J Comput Phys 296:348–368

Islam MA, Deighan D, Bhattacharjee S, Tantalo D, Singh PK, Salac D, Faghihi D (2025) Stochastic deep learning surrogate models for uncertainty propagation in microstructure-properties of ceramic aerogels. Comput Mater Sci 258:114035

Jain RK, Martin JD, Stylianopoulos T (2014) The role of mechanical forces in tumor growth and therapy. Annu Rev Biomed Eng 16(1):321–346

Kapteyn MG, Chaudhuri A, Lima EA, Pash G, Bravo R, Willcox KE, Yankeelov TE, Hormuth DA II (2026) Tumortwin: a python framework for patient-specific digital twins in oncology. BMC Med Inform Decis Mak

Kim K-T, Villa U, Parno M, Marzouk Y, Ghattas O, Petra N (2023) hippylib-muq: A bayesian inference software framework for integration of data with complex predictive models under uncertainty. ACM Trans Math Softw 49(2):1–31

Liang B, Tan J, Lozenski L, Hormuth DA, Yankeelov TE, Villa U, Faghihi D (2023) Bayesian inference of tissue heterogeneity for individualized prediction of glioma growth. IEEE Trans Med Imaging 42(10):2865–2875

Lima E, Oden J, Hormuth D, Yankeelov T, Almeida R (2016) Selection, calibration, and validation of models of tumor growth. Math Models Methods Appl Sci 26(12):2341–2368

Lucci G, Agosti A, Ciarletta P, Giverso C (2022) Coupling solid and fluid stresses with brain tumour growth and white matter tract deformations in a neuroimaging-informed model. Biomech Model Mechanobiol 21(5):1483–1509

Mascheroni P, Stigliano C, Carfagna M, Boso DP, Preziosi L, Decuzzi P, Schrefler BA (2016) Predicting the growth of glioblastoma multiforme spheroids using a multiphase porous media model. Biomech Model Mechanobiol 15(5):1215–1228

Mihai LA, Budday S, Holzapfel GA, Kuhl E, Goriely A (2017) A family of hyperelastic models for human brain tissue. J Mech Phys Solids 106:60–79

Mpekris F, Angeli S, Pirentis AP, Stylianopoulos T (2015) Stress-mediated progression of solid tumors: effect of mechanical stress on tissue oxygenation, cancer cell proliferation, and drug delivery. Biomech Model Mechanobiol 14(6):1391–1402

Padhani AR, Liu G, Mu-Koh D, Chenevert TL, Thoeny HC, Takahara T, Dzik-Jurasz A, Ross BD, Van Cauteren M, Collins D et al (2009) Diffusion-weighted magnetic resonance imaging as a cancer biomarker: consensus and recommendations. Neoplasia 11(2):102–125

Pash G, Villa U, Hormuth DA, II, Yankeelov TE, Willcox K (2026) Predictive digital twins with quantified uncertainty for patient-specific decision making in oncology. J Comput Phys 114937

Pinski FJ, Simpson G, Stuart AM, Weber H (2015) Algorithms for kullback-leibler approximation of probability measures in infinite dimensions. SIAM J Sci Comput 37(6):A2733–A2757

Roininen L, Huttunen JM, Lasanen S (2014) Whittle-matérn priors for bayesian statistical inversion with applications in electrical impedance tomography., Inverse Problems & Imaging 8 (2)

Singh PK, Faghihi D (2025) Chance-constrained optimal design of porous thermal insulation systems under spatially correlated uncertainty. Struct Multidiscip Optim 68(9):178

Singh PK, Farrell-Maupin KA, Faghihi D (2024) A framework for strategic discovery of credible neural network surrogate models under uncertainty. Comput Methods Appl Mech Eng 427:117061

Stylianopoulos T, Martin JD, Snuderl M, Mpekris F, Jain SR, Jain RK (2013) Coevolution of solid stress and interstitial fluid pressure in tumors during progression: implications for vascular collapse. Can Res 73(13):3833–3841

Sugahara T, Korogi Y, Kochi M, Ikushima I, Shigematu Y, Hirai T, Okuda T, Liang L, Ge Y, Komohara Y et al (1999) Usefulness of diffusion-weighted mri with echo-planar technique in the evaluation of cellularity in gliomas, Journal of Magnetic Resonance Imaging: An Official Journal of the International Society for. Magn Reson Med 9(1):53–60

Swanson KR, Alvord EC Jr, Murray JD (2000) A quantitative model for differential motility of gliomas in grey and white matter. Cell Prolif 33(5):317–329

Tan J, Faghihi D (2024) A scalable framework for multi-objective pde-constrained design of building insulation under uncertainty. Comput Methods Appl Mech Eng 419:116628

Tunç B, Hormuth DA II, Biros G, Yankeelov TE (2021) Modeling of glioma growth with mass effect by longitudinal magnetic resonance imaging. IEEE Trans Biomed Eng 68(12):3713–3724

Villa U, Petra N, Ghattas O (Apr. 2021) HIPPYlib: An Extensible Software Framework for Large-Scale Inverse Problems Governed by PDEs: Part I: Deterministic Inversion and Linearized Bayesian Inference, ACM Trans. Math. Softw. 47 (2). https://doi.org/10.1145/3428447

Villa U, Petra N, Ghattas O (2018) hIPPYlib: an Extensible Software Framework for Large-scale Deterministic and Bayesian Inverse Problems. Journal of Open Source Software 3(30). https://doi.org/10.21105/joss.00940

Villa U, Petra N, Ghattas O (2016) hIPPYlib: an Extensible Software Framework for Large-scale Deterministic and Bayesian Inverse Problems. https://doi.org/10.5281/zenodo.596931 http://hippylib.github.io

Wong KC, Summers R, Kebebew E, Yao J (2014) Tumor growth prediction with hyperelastic biomechanical model, physiological data fusion, and nonlinear optimization, in: International Conference on Medical Image Computing and Computer-Assisted Intervention, Springer, pp. 25–32

Publisher's Note Springer Nature remains neutral with regard to jurisdictional claims in published maps and institutional affiliations.